16 Medical Uses of X-Rays

X-rays are used to obtain diagnostic information and for cancer therapy. They are photons of electromagnetic radiation with higher energy than photons of visible light. Gamma rays are photons emitted by radioactive nuclei; except for their origin, they are identical to x-ray photons of the same energy. Section 16.1 describes the production of x-rays. Section 16.2 introduces some new quantities that are important for measuring how the absorbed photon energy relates to the response of a detector—which might be a film, an ionization chamber, or a chemical detector. Several detectors are introduced in Sect. 16.3: film, fluorescent screens, scintillation detectors, semiconductor detectors, thermoluminescent dosimeters (TLD), and digital detectors. Section 16.4 describes the diagnostic radiograph, and the following section discusses image quality, particularly the importance of noise in determining image quality. Section 16.6 provides a brief mention of angiography, and Sect. 16.7 discusses some of the special problems of mammography. Computed tomography with x-rays is discussed in Sect. 16.8. The final sections deal with the biological effects of x-rays, cancer therapy, dose, and the risk of radiation.

16.1 Production of X-Rays

When a beam of energetic electrons stops in a target x-rays are emitted. *Characteristic x-rays* have discrete photon energies and are produced after excitation of an atom by the electron beam. *Bremsstrahlung* (Sect. 15.11) is the continuous spectrum of photon energies produced when an electron is scattered by an atomic nucleus. Bremsstrahlung is responsible for most of the photons emitted by most x-ray tubes. The total bremsstrahlung radiation yield as a function of electron energy for various materials is shown in Fig. 16.1. High-Z materials are most efficient for producing x-rays. Tungsten ($Z = 74$) is often used as a target in x-ray tubes because it has a high radiation yield and can withstand high temperatures. For 100-keV electrons on tungsten, the radiation yield is about 1 %: most of the electron energy heats the target. We now consider these two processes in greater detail.

16.1.1 Characteristic X-Rays

Atomic energy levels are described in Sect. 14.3. The levels for tungsten are shown in Table 15.1 and Fig. 15.1. An electron bombarding a target can impart sufficient energy to a target electron to remove it from the atom, leaving an unoccupied energy level or *hole*. The deexcitation of the atom is described in Sect. 15.9. For a high-Z material with a hole in the K shell, the fluorescence yield is large (see Fig. 15.14). The hole is usually filled when an electron in a higher energy level drops down to the unoccupied level. As it does so, the atom emits a characteristic x-ray—a photon with energy equal to the difference in energies of the two levels. This leaves a new hole, which is then filled by an electron from a still higher level with the emission of another x-ray, or by an Auger cascade.

As a hole moving to larger values of n corresponds to a decrease of the total energy of the atom, it is customary to draw the energy-level diagram for holes instead of electrons, which turns the graph upside down, as in Fig. 16.2. The zero of energy is the neutral atom in its ground state. As this is a logarithmic scale, zero cannot be shown.

Creation of the hole requires energy to remove an electron. That energy is released when the hole is filled. Various possible transitions are indicated in Fig. 16.2. These transitions are consistent with these selection rules, which can be derived using quantum theory:

$$\Delta l = \pm 1, \qquad \Delta j = 0, \pm 1. \qquad (16.1)$$

The transitions are labeled by the letters K, L, M, and so forth, depending on which shell the hole is in initially. Greek-letter subscripts distinguish the x-rays from transitions to different final states.

R. K. Hobbie, B. J. Roth, *Intermediate Physics for Medicine and Biology*,
DOI 10.1007/978-3-319-12682-1_16, © Springer International Publishing Switzerland 2015

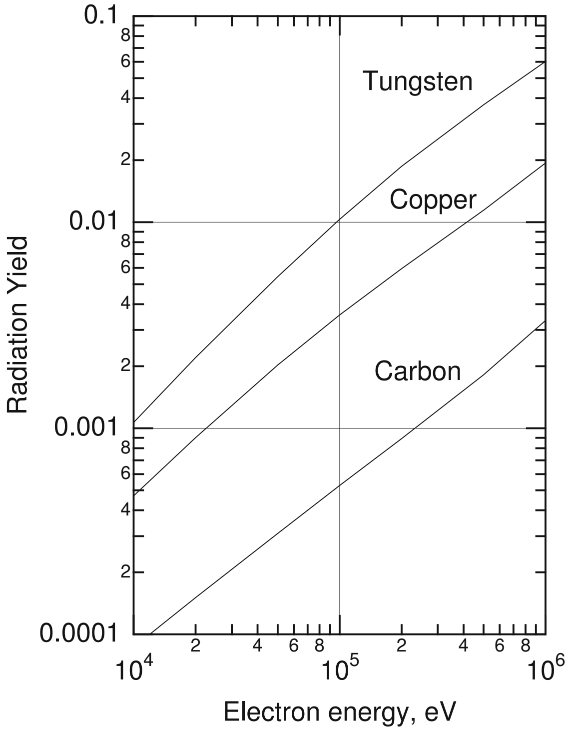

Fig. 16.1 Radiation yield vs. electron energy for carbon, copper, and tungsten. Plotted from data in ICRU Report 37 (1984). The radiation yield is the fraction of the electron's energy that is converted to photon energy; see Sect 15.13

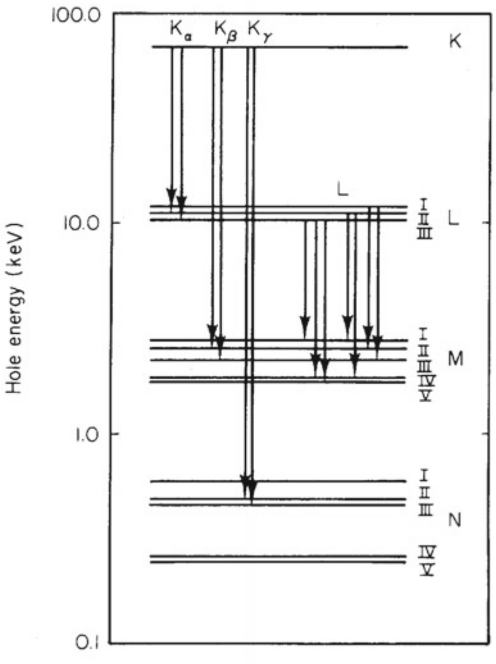

Fig. 16.2 Energy-level diagram for holes in tungsten and some of the x-ray transitions

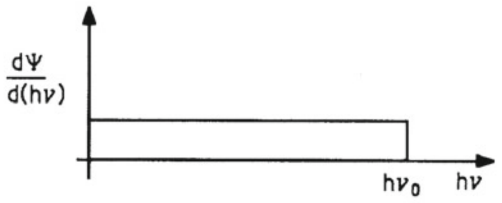

Fig. 16.3 The energy fluence spectrum of bremsstrahlung x-rays emitted when monoenergetic electrons strike a thin target

Analogous to the approximate formula of Eq. 15.2 is the following estimate of the energy of the K_α line (which depends on the screening for two values of n), which we have seen before as Eq. 15.33:

$$E_{K_\alpha} = \tfrac{3}{4}(13.6\,\text{eV})(Z-1)^2. \tag{16.2}$$

The factor 3/4 is what one would have for hydrogen if $n_i = 2$ and $n_f = 1$ are substituted in the Bohr formula, Eq. 14.9. The screening also depends strongly on l.

16.1.2 Bremsstrahlung

The other mechanism for x-ray production is the acceleration of electrons in the Coulomb field of the nucleus, described in Sect. 15.11. Classically, a charged particle at rest creates an electric field that is inversely proportional to the square of the distance from the charge. When in motion with a constant velocity, it creates both an electric field and a magnetic field. When accelerated, additional electric and magnetic fields appear that fall off less rapidly—inversely with the first power of distance from the charge. This is classical electromagnetic radiation. Quantum mechanically, when a charged particle undergoes acceleration or deceleration, it emits photons. The radiation is called deceleration radiation, braking radiation, or *bremsstrahlung*. It has a continuous distribution of frequencies up to some maximum value.

The photon *energy* fluence spectrum of bremsstrahlung radiation from monoenergetic electrons passing through a thin target is constant from a maximum energy $h\nu_0$ down to zero, as shown in Fig. 16.3 (Attix 1986, p. 212). The maximum frequency is related to the kinetic energy of the electrons by $T = h\nu_0$, as one would expect from conservation of energy. (A photon of energy $h\nu_0$ is emitted when an electron loses all of its energy in a single collision).

For a thick target, we assume that all electrons at the same depth have the same energy (that is, we ignore straggling), and we ignore attenuation of photons coming out of the target. The spectrum is then the integral of a number of spectra

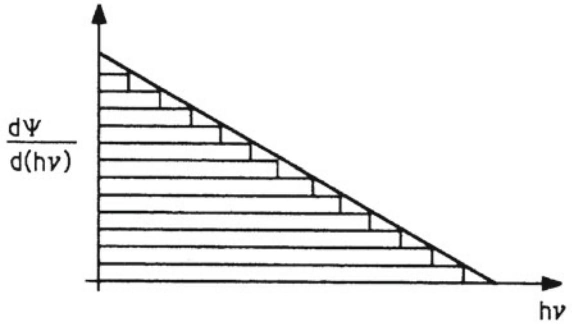

Fig. 16.4 The energy fluence spectrum of bremsstrahlung x-rays from a thick target, ignoring absorption of the photons in the target. The form is $d\Psi/d(h\nu) = CZ(h\nu_0 - h\nu)$

like that in Fig. 16.3. The thick-target spectrum is shown in Fig. 16.4. The spectral form is

$$\frac{d\Psi}{d(h\nu)} \equiv \frac{d\Psi}{dE} = CZ(h\nu_0 - h\nu) = CZ(T - E). \quad (16.3a)$$

The photon particle fluence spectrum is

$$\frac{d\Phi}{dE} = \frac{1}{h\nu}\frac{d\Psi}{dE} = CZ\left(\frac{h\nu_0}{h\nu} - 1\right). \quad (16.3b)$$

More of the low-energy photons that are generated within the target are attenuated as they escape, because of the much larger values of the attenuation coefficient at low energies (recall Figs. 15.10 and 15.11). This cuts off the low-energy end of the spectrum. If the electron energy is high enough, the discrete spectrum due to characteristic fluorescence is superimposed on the continuous bremsstrahlung spectrum. Both of these effects are shown in Fig. 16.5, which compares calculations and measurements of the particle fluence spectrum $d\Phi/dE$.

16.2 Quantities to Describe Radiation Interactions: Radiation Chemical Yield, Mean Energy Per Ion Pair, and Exposure

Section 15.15 introduced the quantities energy transferred, energy imparted, kerma, and absorbed dose, which are used to describe radiation and its effects. This section introduces some additional quantities (ICRU Report 33 1980, Reprinted 1992) that are used to describe the interaction of the radiation with the detectors discussed in Sect. 16.3.

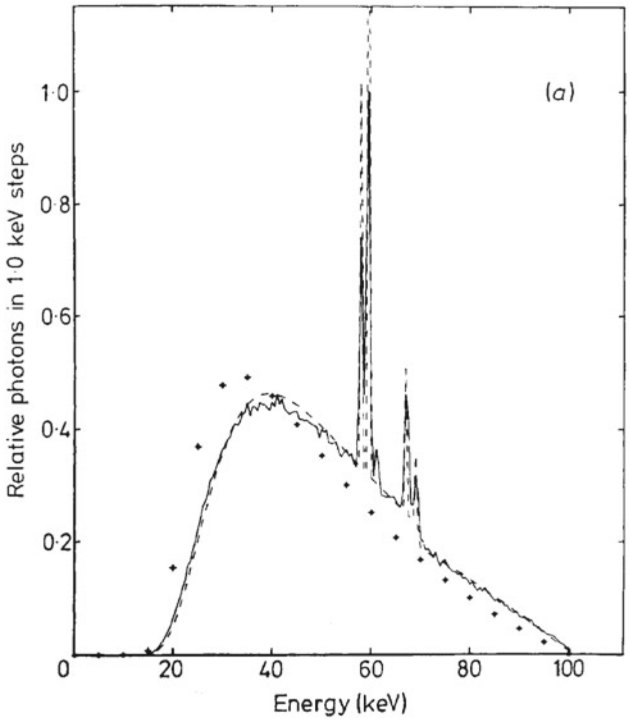

Fig. 16.5 Theoretical and measured photon particle spectra, $d\Phi/d(h\nu)$, for 100-keV electrons striking a thick tungsten target. The solid line represents measurements with a high-resolution semiconductor detector. The dashed line is the theory of Birch and Marshall (1979), which takes photon absorption into account. The crosses show an earlier theoretical model. (From Birch and Marshall 1979. Used by permission of the Institute of Physics)

16.2.1 Radiation Chemical Yield

The *radiation chemical yield G* of a substance is the mean number of moles $\overline{n}$ of the substance produced, destroyed, or changed in some volume of matter, divided by the mean energy imparted to the matter:

$$G = \frac{\overline{n}}{\overline{E}}. \quad (16.4)$$

Its units are mol J^{-1}. (A related quantity expressed in non-SI units is the *G value*, expressed in molecules or moles per 100 eV of energy imparted.) The radiation chemical yield is particularly useful for describing chemical dosimeters. These are usually dilute aqueous solutions, so the radiation chemical yield of water is the important parameter.

16.2.2 Mean Energy per Ion Pair

Other detectors measure ionization produced in a gas by the radiation. The *mean energy expended in a gas per ion pair*

Table 16.1 Some representative values of the average energy per ion pair, W

Gas	W (eV per ion pair for electrons[a])
He	41.3
Ar	26.4
Xe	22.1
Air	33.97[b]
Semiconductors	W (eV per electron-hole pair)
Si	3.68
Ge	2.97

[a] From ICRU Report 31 (1979)

[b] ICRU Report 39 (1979) recommends 33.85 J C^{-1}. Attix (1986) uses 33.97 J C^{-1}. Note that 1 J C^{-1} is equivalent to 1 eV per singly-charged ion pair

formed, W, is

$$W = \frac{T_0}{\overline{N_i}}, \tag{16.5}$$

where T_0 is the initial kinetic energy of a charged particle and $\overline{N_i}$ is the mean number of ion pairs formed when T_0 is completely dissipated in the gas. The units are joules or electron volts per ion pair. The mean energy expended per ion pair is not equal to the ionization energy. To see why, consider three processes that can take place. The first is ionization, with $\overline{E}_i$ being the average energy of an ionized atom. Second, the collision may promote an atomic electron to an excited state without ionization. The average excitation energy is $\overline{E}_{\text{ex}}$. Finally, the charged particle may lose energy without producing ionization, a process called *subexcitation*. The average subexcitation energy is defined to be the energy lost by this process, E_{se}, divided by $\overline{N}_i$. Conservation of energy for this model leads to

$$T_0 = \overline{N}_i \overline{E}_i + \overline{N}_{\text{ex}} \overline{E}_{\text{ex}} + \overline{N}_i \overline{E}_{\text{se}}.$$

Dividing each term by $\overline{N}_i$ leads to an expression for W. In general, W is determined experimentally, because the terms in this equation are quite difficult to calculate. However, they have been calculated for helium.[1] The mean energy of an ionized helium atom is only 62 % of the value of W:

$$\underbrace{W}_{41.8\ \text{eV}} = \underbrace{\overline{E}_i}_{\substack{25.9\ \text{eV} \\ 62\,\%}} + \underbrace{\left(\overline{N}_{\text{ex}}/\overline{N}_i\right)\overline{E}_{\text{ex}}}_{\substack{0.4\times 20.8=8.3\ \text{eV} \\ 20\%}} + \underbrace{\overline{E}_{\text{se}}}_{\substack{7.6\ \text{eV} \\ 18\,\%}}$$

Values of W are tabulated in ICRU Report 31 (1979). There are variations of a few percent depending on whether the charged particle is an electron or an α particle. Table 16.1 provides a few representative values. Though defined for a gas, W is also applied to semiconductors as the average energy per electron–hole pair produced. Values of W for semiconductors are much smaller than for a gas.

16.2.3 Exposure

The *exposure* X is defined only for photons and measures the energy fluence of the photon beam. It is the amount of ionization (total charge of one sign) produced per unit mass of dry air when all of the electrons and positrons liberated in a small mass of air are completely stopped in air:

$$X = \frac{dq}{dm}. \tag{16.6}$$

The units are coulomb per kilogram. Since the average amount of energy required to produce an ion pair is well defined, exposure is closely related to collision kerma in air. The definition of X does not include ionization arising from the absorption of bremsstrahlung emitted by the electrons, so there is a slight difference at high energies.[2] The relationship is

$$X = (K_c)_{\text{air}} \left(\frac{e}{W_{\text{air}}}\right) = \Psi \left(\frac{\mu_{\text{en}}}{\rho}\right)_{\text{air}} \left(\frac{e}{W_{\text{air}}}\right). \tag{16.7}$$

If charged-particle equilibrium exists, the dose in air is related to the beam energy fluence by Eqs. 15.71 and 15.74:

$$D_{\text{air}} = \left(\frac{\mu_{\text{en}}}{\rho}\right)_{\text{air}} \Psi.$$

The dose for the same energy fluence in some other medium is

$$D_{\text{med}} = \left(\frac{\mu_{\text{en}}}{\rho}\right)_{\text{med}} \Psi = \frac{(\mu_{\text{en}}/\rho)_{\text{med}}}{(\mu_{\text{en}}/\rho)_{\text{air}}} D_{\text{air}}. \tag{16.8}$$

The *roentgen* (R) is an old unit of exposure equivalent to the production of 2.58×10^{-4} C kg^{-1} in dry air; this corresponds to a dose of 8.69×10^{-3} Gy. (The relationship is developed in Problem 7).

16.3 Detectors

Detectors are used for recording an image and also for measuring the amount of radiation to which a patient is exposed. This section describes the most common kinds of detectors.

---

[1] See Platzman (1961); also Attix (1986, pp. 339–343).

[2] There is also a problem at high energies because the range of the electrons is large. If they are to come to rest within the chamber, the size of the chamber becomes comparable to the photon attenuation coefficient.

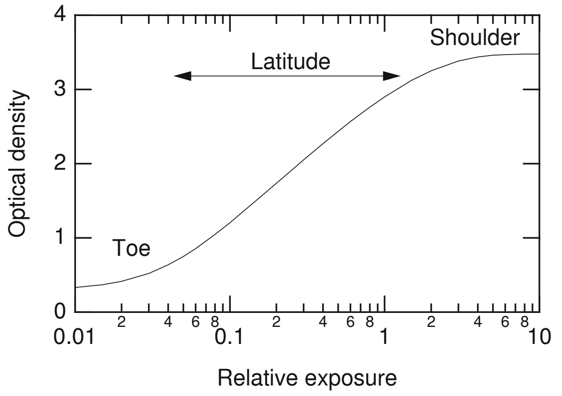

Fig. 16.6 Optical density vs. the logarithm of the relative exposure for a hypothetical x-ray film

16.3.1 Film and Screens

Film was the original x-ray detector used by Wilhelm Roentgen, the discoverer of x-rays. For years it was the most common detector for diagnostic radiology. In recent years it has been replaced by digital detectors. We describe it briefly for comparison with the newer techniques.

A typical x-ray film has a transparent base about 200 μm thick, coated on one or both sides with a sensitive emulsion containing a silver halide (usually silver bromide). We will not discuss the rather complicated sequence of steps by which the absorption of photons or energy loss by charged particles leads to a latent or developable image in the film. When the film is developed, the emulsion grains that have absorbed energy are reduced to black specks of metallic silver. The film is then fixed, a process in which the silver halide that was not reduced is removed from the emulsion. The result is a film that absorbs visible light where it was struck by ionizing radiation.

The fraction of incident light passing through the film after development is called the *transmittance*, T. The *optical density* or *density* is defined to be

$$\mathrm{OD} = \log_{10}(1/T). \tag{16.9}$$

A film that transmits 1 % of the incident viewing light has an optical density of 2.

The response of a film is described by plotting the optical density against the log of the exposure in air immediately in front of the film (or equivalently, the absorbed dose in the film emulsion). Since the optical density is the logarithm of the transmittance, this is a log–log plot of the reciprocal of the fraction of the visible light transmitted when viewing the processed film vs. the x-ray exposure before processing. A typical plot of film response is shown in Fig. 16.6. If the curve is linear, the transmittance is proportional to the exposure raised to some power:

$$T \propto X^{-\gamma}.$$

At very small exposures (the *toe*) the transmission is that of the base and "clear" emulsion. At very high exposures (the *shoulder*) all of the silver halide has been reduced to metallic silver, and the film has its maximum optical density. In between is a region that is almost linear (on a log–log scale). The ratio of maximum to minimum usable exposure is called the *latitude* of the film. The largest value of the exponent occurs at the inflection point and is called the *gamma* or *contrast* of the film. Both the exponent and the position of the curve along the log exposure axis depend on the development time, the temperature of the developing solution, and the energy of the x-ray beam. The *film speed* is the reciprocal of the exposure required for an optical density that is 1 greater than the base density.

A typical film has an emulsion containing AgBr. It requires a dose of 1.74×10^{-4} Gy (J kg^{-1}) in air just in front of the film to produce an optical density of 1. This might be where the body is not blocking the beam. The smaller dose to the film where there has been significant attenuation in the body gives a lighter region, as in the heart and bone shadows of Fig. 16.17.

The dose to the part of the body just in front of the film (the *exit dose* to the patient) can be written in several ways. For simplicity we assume monoenergetic photons. In terms of the energy fluence of the photon beam, the exit dose is

$$D_{\text{body}} = \left(\frac{\mu_{\text{en}}}{\rho}\right)_{\text{body}} \Psi. \tag{16.10a}$$

In terms of the dose in air just in front of the film it is

$$D_{\text{body}} = \frac{(\mu_{\text{en}}/\rho)_{\text{body}}}{(\mu_{\text{en}}/\rho)_{\text{air}}} D_{\text{air}}, \tag{16.10b}$$

and in terms of the dose in the film it is

$$D_{\text{body}} = \frac{(\mu_{\text{en}}/\rho)_{\text{body}}}{(\mu_{\text{en}}/\rho)_{\text{film}}} D_{\text{film}}. \tag{16.10c}$$

For 50-keV photons we find from the tables at physics.nist.gov/PhysRefData/XrayMassCoef/ that $(\mu_{\text{en}}/\rho)_{\text{muscle}}/(\mu_{\text{en}}/\rho)_{\text{air}} = 0.004\,349/0.004\,098 = 1.061$. Therefore the exit dose would be $(1.74 \times 10^{-4})(1.061) = 1.85 \times 10^{-4}$ Gy. Because of attenuation, the entrance dose can be much larger.

The dose can be reduced by a factor of 50 or more if the film is sandwiched between two fluorescent *intensifying screens*. The x-ray photons have a low probability of interacting in the film. The screens have a greater probability of absorbing the x-ray photons and converting them to visible light, to which the film is more sensitive. For 50-keV photons on typical emulsion, the value of μ_{en}/ρ is about 0.261 m^2 kg^{-1}. A typical value of $\rho \Delta x$ for the film might be 0.02 kg m^{-2}. Therefore $\mu_{en} \Delta x = 0.0052$. The fraction of incident energy absorbed in the emulsion is $1 - e^{-0.0052} = 0.0052$.

A typical screen might consist of particles of terbium-doped gadolinium oxysulfide (Gd_2O_2S:Tb) suspended in a carrier about 150 µm thick (0.5–1.5 kg m^{-2}). This layer is backed by a thin reflective layer. Two such screens (one on each side of the film) with a total thickness of 1.2 kg m^{-2} absorb 28 % of the 50-keV photons that pass through them (see Problem 11). The overall effect is to produce the same optical density when the energy fluence in the x-ray beam is reduced by a factor of 54—the ratio of the incident radiation absorbed in the screen and in the film in each case.[3] Typically, a sheet of film is placed in a light-tight *cassette* whose front and back walls are made of screen material.

Figure 16.6 shows a plot of optical density vs. the log of the exposure. The slope at any point on the curve is[4]

$$\gamma = \frac{d \log_{10}(1/T)}{d \log_{10} X} = \frac{d \ln(1/T)}{d \ln X} = -\frac{dT/T}{dX/X}$$
$$= -\frac{X}{T}\frac{dT}{dX} = -\frac{1}{G}g, \qquad (16.11)$$

where $G = T/X$ is the *large-signal transfer factor* and $g = dT/dX$ is the *incremental-signal transfer factor*. This will be used in our discussion of detecting signals in noise in the next section.

16.3.2 Scintillation Detectors

When x-ray photons interact with matter, some of their energy is transferred to electrons. These electrons interact in turn, and some of their energy can become ultraviolet or visible photons. A *scintillator* is a substance that produces these photons with high efficiency, yet is transparent to them. The photons are then transferred by an optical fiber or a lens system to a light detector such as a photomultiplier tube or a solid-state photodetector. Each x-ray photon produces an electrical current pulse at the detector output, called a *count*. When the number of counts is recorded vs. the pulse height (total charge in the pulse, which is proportional to the energy deposited in the scintillator), the result is a *pulse-height spectrum*. For monoenergetic photons, the ideal pulse height spectrum would consist of a single peak: all pulses would have the same height. This is not realized in practice for two reasons: statistical variations in the scintillation process cause the line to be broadened, and the entire energy of the incident photon is not converted into electrons.

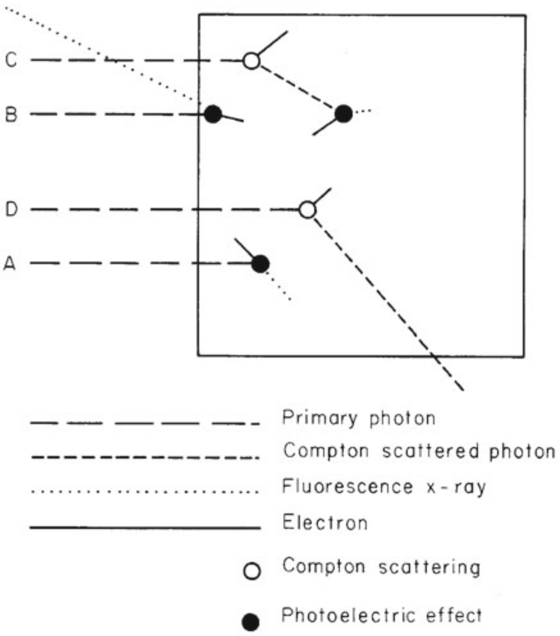

Fig. 16.7 Mechanisms by which some of the energy of a primary photon can escape from a detector. Photons *A* and *B* undergo photoelectric absorption. All of the energy from *A* is absorbed in the detector, while the fluorescence x-ray from *B* escapes. Photons *C* and *D* are Compton scattered. The scattered photon from *C* undergoes subsequent absorption, while that from *D* escapes

An atom that has been excited by photoelectric absorption can decay by the emission of a fluorescence photon. If this photon is subsequently absorbed in the scintillator, all of the original photon energy is converted to electron energy so rapidly that the visible light is all part of one pulse. The pulse height then corresponds to the full energy of the original photon. However, if the initial photoelectric absorption takes place close to the edge of the detector, the fluorescence photon can escape, and the pulse has a lower height than those in the primary peak. This can be seen in Fig. 16.7. Photons *A* and *B* interact by photoelectric effect. All the energy for photon *A* is deposited in the scintillator, while the *K* fluorescence photon from *B* escapes. The effect on a pulse height spectrum is shown in Fig. 16.8 for a scintillator of sodium iodide.

In Compton scattering, the energy of the recoil electron is transferred to the scintillator (unless the electron escapes).

---

[3] The fluorescent radiation has a wavelength of about 545 nm (green), and each absorbed high-energy photon has sufficient energy to produce about 14,000 fluorescence photons. However, the efficiency of production is only about 5 % so 700 photons are produced. Some of these escape or are absorbed. Each x-ray photon produces about 150 photons of visible and ultraviolet light that strike the emulsion—more than enough to blacken the film in the region where the x-ray photon was absorbed by the screen.

[4] An argument based on Eq. 2.14 can be used to show that $\log_{10} x = (1/2.303) \ln x = 0.43 \ln x$.

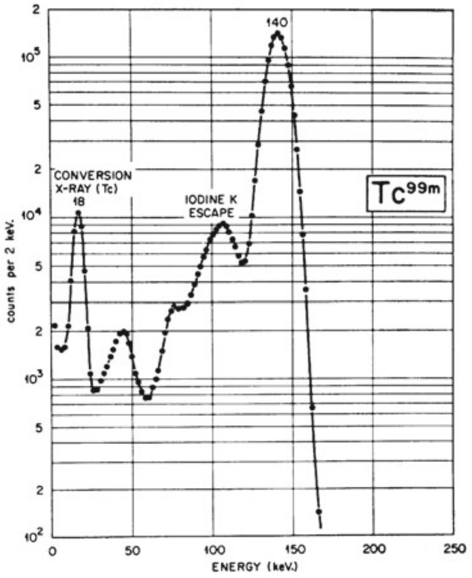

Fig. 16.8 Spectrum of pulse heights for 140-keV photons from isotope $^{99\mathrm{m}}$Tc incident on a sodium iodide scintillator. The 140-keV total energy peak is prominent, as is the peak at 110 keV corresponding to the escape of the *K* fluorescence x-ray from iodine. The Compton scatter continuum runs from 49 keV down to zero energy. The peak at 18 keV is from additional radiation from $^{99\mathrm{m}}$Tc (see Chap. 17; Reproduced from Wagner 1968, p. 162. Copyright 1968 by W. B. Saunders. Used by permission of Elsevier)

The scattered photon may escape from the detector, as in *D* of Fig. 16.7. (If it is subsequently absorbed, as in mechanism *C* of Fig. 16.7, the pulse height will have the peak value). The energy of the recoil electron is given by Eq. 15.15. The maximum electron energy occurs when the photon is scattered through $\theta = 180\,°$. Then

$$T_{\max} = \frac{2h\nu_0 x}{1+2x} = \frac{(h\nu_0)^2}{h\nu_0 + m_e c^2/2}.$$

If the photon energy is in keV, this is

$$T_{\max} = \frac{(h\nu_0)^2}{h\nu_0 + 256}. \tag{16.12}$$

A pulse-height spectrum for "pure" Compton scattering of 662-keV photons (as emitted by ^{137}Cs) is shown in Fig. 16.9. The peak of the Compton continuum is at $T_{\max} = (662)^2/(662 + 256) = 477$ keV. The cases of perfect resolution with complete absorption and real resolution with complete absorption are shown, along with the theoretical Compton continuum with perfect resolution, and a real spectrum.

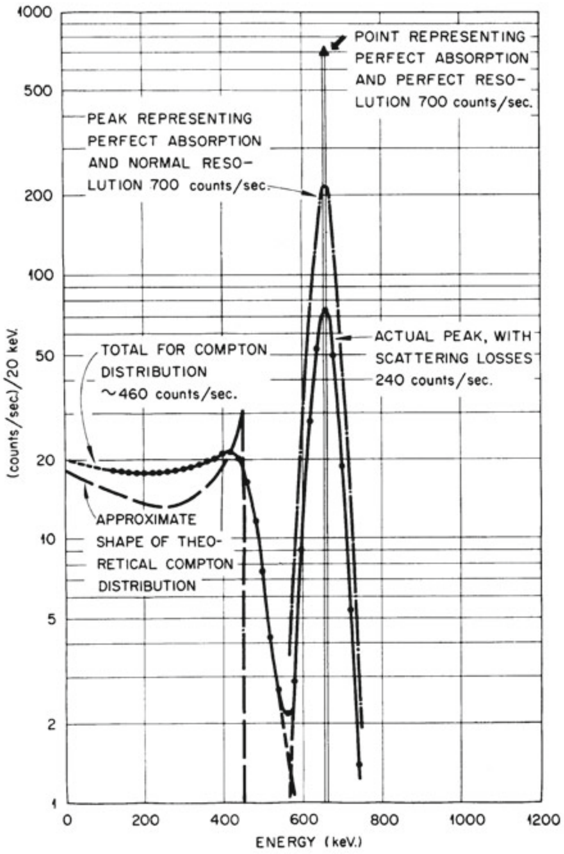

Fig. 16.9 The response of a sodium iodide detector to 662-keV photons from ^{137}Cs. Theoretical responses are shown for a detector that absorbs the energy of all photons and has perfect resolution, for a detector with perfect absorption and finite resolution, and for a detector in which Compton-scattered photons can escape. Experimental data are for a $1\frac{1}{2}$-in. by 1-in. NaI crystal. (Redrawn from Harris et al. 1969; Reproduced from Wagner 1968, p. 153. Copyright 1968 W. B. Saunders. Used by permission of Elsevier)

When the energy of the primary photons is so large that pair production is important, an additional escape mechanism must be considered. We know (Eq. 15.22) that

$$h\nu_0 = T_+ + T_- + (m_e c^2)_{e^-} + (m_e c^2)_{e^+}.$$

The positron will eventually combine with another electron to produce two annihilation radiation photons:

$$(m_e c^2)_{e^+} + (m_e c^2)_{\text{another } e^-} = 2E_\gamma.$$

The energy of each annihilation photon is 511 keV. The initial photon energy is finally distributed as

$$h\nu_0 = T_+ + T_- + \gamma(511) + \gamma(511).$$

If all this energy is absorbed in the detector, the pulse height corresponds to the full energy of the incident photon. One

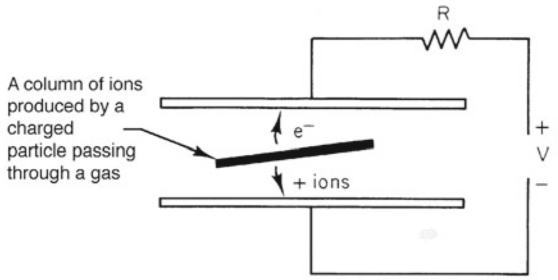

Fig. 16.10 Schematic of an ionization chamber or proportional counter. The ions discharge the capacitor, which is recharged between counts through resistor R

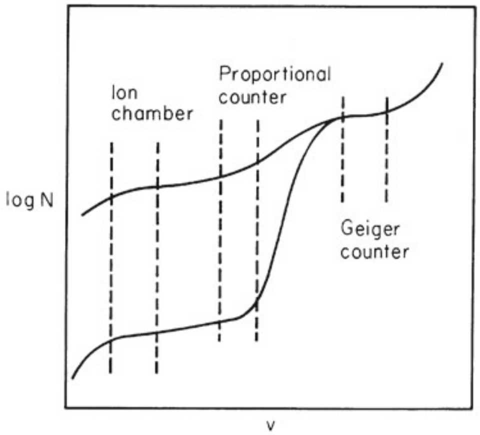

Fig. 16.11 The number of ions collected vs. collecting potential for two particles that deposit different amounts of energy in a gas detector. The voltage regions are indicated where the device operates as an ionization chamber, a proportional counter, and a Geiger counter

or both of the annihilation photons can escape, giving the one-photon escape peak and the two-photon escape peak.

Scintillation detectors vary greatly in size. Large ones may be tens of centimeters in diameter; others can be less than a millimeter. A large number of materials are used (van Eijk 2002).

16.3.3 Gas Detectors

Ionization in gas is the basis for three kinds of x-ray detectors: ionization chambers, proportional counters, and Geiger counters. A photon passing through a gas can produce photoelectric, Compton, or pair-production electrons. These then lose energy by electron collisions. Ion pairs are produced in the gas, the average number being proportional to the amount of energy lost in the gas. The average amount of energy required to produce an ion pair is W, as we saw in Sect. 16.2. Imagine that the ions are produced between the plates of a charged capacitor as shown in Fig. 16.10. The electrons are attracted to the positive plate and the positive ions travel to the negative plate. If all the electrons and ions are captured, the total charge collected on each plate has magnitude $q = Ne$, where e is the charge on the electron or ion and N is the number of ion pairs formed. If the capacitance is C, the change in voltage is $\delta v = q/C = Ne/C$. Such a device is called an *ionization chamber*. The cumulative discharge of the capacitor is measured in some pocket dosimeters; in other cases, the capacitor is slowly recharged through a large resistance R so that each photon detected generates a voltage pulse of height δv.

A certain minimum voltage between the two plates is necessary to ensure that all the ions produced are collected, corresponding to the ion chamber region of Fig. 16.11. The ionization chamber is the "workhorse" detector for accurately measuring radiation dose.

If the potential on the plates is raised further, the number of ions collected increases. Between collisions the electrons and ions are accelerated by the electric field, and they acquire enough kinetic energy to produce further ionizations when they collide with molecules of the gas, a process called *gas multiplication*. At moderate potentials, the multiplication factor is independent of the initial ionization, so the number of ions collected is larger than that in an ionization chamber but still is proportional to the initial number of ions. In this region of operation the device is called a *proportional counter*. Parallel-plate geometry is not used in a proportional counter. One electrode is a wire, and the other is a concentric cylinder.

At still higher values of the applied voltage, pulse size is independent of the initial number of ion pairs. In this mode of operation, the device is called a *Geiger counter*.

Any gas detector used to detect high-energy photons suffers from the fact that the gas is not very dense. At low energies the photoelectric cross-section is high and most photons interact. At higher energies, many photons pass through the gas and detector walls without interacting. A thin sheet of absorber in front of the gas detector can actually increase the counting rate. An example is shown in Fig. 16.12. The detector had an aluminum wall of thickness 0.3 kg m^{-2}. Electrons of 125 keV or more pass completely through the detector wall. The maximum energy of Compton electrons from the 1.1-MeV photons is 890 keV. Compton electrons produced in a thin layer of lead can pass through the aluminum and ionize the gas in the detector. Once the total thickness of lead and aluminum is sufficient to stop all the Compton electrons, the addition of more lead upstream does not increase the detector efficiency, and exponential attenuation is seen.

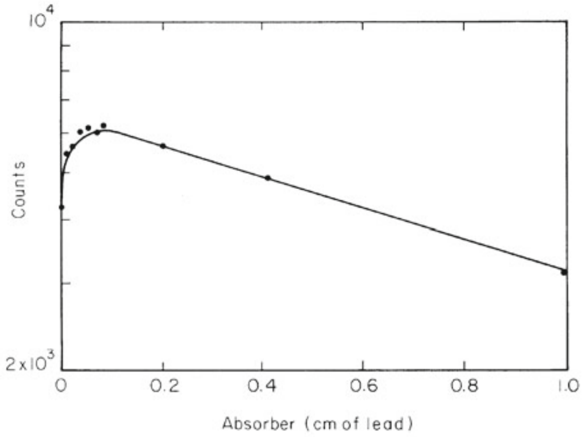

Fig. 16.12 Counting rate of a Geiger counter vs. the thickness of a lead absorber in front of the detector, showing the buildup of counting rate due to the conversion of photons to electrons in the lead by Compton scattering. These electrons pass through the thin wall of the counter and ionize the gas. The photons were from ^{60}Co and had an energy of 1.1 MeV

16.3.4 Semiconductor Detectors

A semiconductor detector is very much like an ionization chamber, except that a solid is used as the detecting medium. The "ion pair" is an electron that has received sufficient energy to be able to leave its atom and move freely within the semiconductor (but not enough energy to leave the semiconductor entirely) and the "hole" that the electron left behind. Electrons from neighboring atoms can fall into the hole, so the hole can move from atom to atom just like a positive charge. Details of the operation of semiconductor detectors can be found in Lutz (1999).

A semiconductor detector has two principal advantages over a gas ionization chamber. First, the amount of energy required to create an electron–hole pair is only about 3 eV, one tenth the value for a typical gas. This means that many more pairs are produced and the statistical accuracy is better. Second, the density of a solid is much greater than the density of a gas, so the probability that a photon interacts is larger. The cross-section for interaction increases with high Z, so detectors made of germanium ($Z = 32$) are better for photon detection than those made of silicon ($Z = 14$). Diode detectors are used for real-time dose measurement in patients receiving radiation therapy (AAPM Report 87 2005).

16.3.5 Thermoluminescent Dosimeters

Thermoluminescent phosphors consist of a small amount of dielectric material (0.1 g or less) that has been doped with impurities or has missing atoms in the crystal lattice to form metastable energy levels or traps. These impurities or defects are far from one another and are isolated in the lattice, so that electrons cannot move freely from one trap to another. When the phosphor is irradiated with ionizing radiation, some of the electrons are trapped in these metastable states. There are levels associated with the material at an energy E above the trap energy (the conduction band) which allow electrons to move throughout the phosphor. The probability that an electron escapes from the trap is proportional to a Boltzmann factor, $\exp(-E/k_B T)$. If E is large enough, the lifetime in the trapped state can be quite long—up to hundreds of years. Heating allows the electrons to escape to the higher levels, where they then fall back to the normal state with the emission of visible photons. Ordinary table salt (NaCl) exhibits this behavior. If it is irradiated and then sprinkled on an electric hot plate in a darkened room, one can see the flashes of light. The light emitted on heating is called *thermoluminescence*. In a *thermoluminescent dosimeter* (TLD), the light emitted is measured with a photomultiplier tube as the temperature is gradually increased. The total amount of light released is proportional to the energy imparted to the phosphor by the ionizing radiation.

Thermoluminescent dosimeter can measure an integrated dose from 10^{-5} to 10^3 Gy. Great care must be taken both in the preparation and reading of the phosphor. Thermoluminescent dosimeter chips are widely used to measure radiation doses because they are small and have the approximate atomic number and atomic weight of tissue. They are often made of LiF. Detailed descriptions are found in Chap. 14 of Attix (1986), and Shani (1991, 2001). (The two editions of Shani complement one another.)

16.3.6 Chemical Dosimetry

When radiation interacts with water, *free radicals* are produced. A free radical, such as H or OH, is electrically neutral but has an unpaired electron. Free radicals promote other chemical reactions. Typically, a dilute indicator of some sort is added to the water. A common dosimeter is the Fricke ferrous sulfate dosimeter. A 1 mM $FeSO_4$ solution is irradiated. The radiation changes the iron from the ferrous (Fe^{2+}) to the ferric (Fe^{3+}) state with a G of about 1.6×10^{-6} mol J^{-1}. The concentration of ferric ion can be measured by absorption spectroscopy. Details are found in Chap. 14 of Attix (1986) and in Shani (1991, 2001). Magnetic resonance imaging (Chap. 18) is also used to measure the amount of ferric ion in the Fricke dosimeter since the relaxation times depend on the ion concentration. This has led to the gel dosimeter which allows a three-dimensional measurement of the dose distribution—useful for planning radiation treatments (Shani 2001, Chap. 9).

Another form of chemical dosimeter is *radiochromic film*. It consists of a thin layer of radiosensitive dye bonded to a mylar base. The dye darkens with radiation. Radiochromic films are sensitive for doses of 1–500 Gy, making them useful for measuring doses in radiation therapy (Shani 2001, Chap. 5).

16.3.7 Digital Detectors

Digital x-ray detectors have replaced film in clinical radiography (Doi 2006; Armato and van Ginneken 2008; Cowen et al. 2008b; Körner et al. 2007; Uffmann and Schaefer-Prokop 2009). A digitally recorded image generally has up to 400 times the dynamic range (latitude) of film. A factor-of-2 error in film exposure,[5] which renders a conventional radiographic image almost useless, is easily tolerated by digital recording.[6] A digitally stored image allows easier retrieval, transmission, manipulation with computer algorithms, and duplication.

A number of techniques are used. In *Computed Radiography* (CR), the image is formed on a plate of phosphor crystals such as barium fluorobromide. Absorption of x-ray photons leaves the BaFBr crystals in a metastable state, like a TLD phosphor. Scanning by a thin laser beam in a horizontal and vertical raster pattern like a television image causes visible light to be emitted by the trapped electrons. The dynamic range of a storage phosphor can be as high as 10^4, compared to about 10^2 for radiographic film (Rowlands 2002).

In *Direct Radiography* (DR) the thin-film transistor (TFT) array technology used in flat-panel computer screens is used to make large detector arrays. The TFT arrays provide the spatial readout. They are combined either with an amorphous selenium photoconductor that converts the x-ray energy to charge (direct conversion), or with a structured scintillator such as a large array of CsI crystals. Each CsI crystal may be as small as 6 μm diameter by 500 μm long.

16.4 The Diagnostic Radiograph

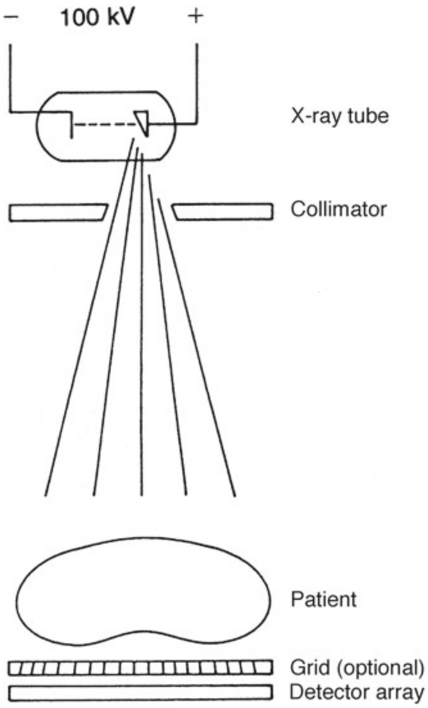

Fig. 16.13 Overall scheme for making a radiograph. Photons are produced when electrons strike the tungsten anode. The beam is collimated to prevent unnecessary dose to the patient. The patient is placed directly in front of the grid (if any), and the digital detector array, which can be film, a sandwich of film and intensifying screen, or a detector array

Figure 16.13 shows the typical elements for making a diagnostic x-ray. An image recorded on film or a detector array is called a *radiograph*. The x-ray tube ideally serves as a point source of photons. The photons are filtered and collimated to illuminate only the portion of the patient of interest. Typically, about 10 % pass through the patient and strike the detector in a chest radiograph. In the abdomen the fraction is about 1 %. There may be an optional grid, as discussed below. We discuss each element below, and then discuss the quality of the image.

16.4.1 X-Ray Tube and Filter

Most routine radiography is done with photons in the range from 35 to 85 keV. (Mammography uses lower energy, and computed tomography is somewhat higher.) Figure 16.14 shows the loss of radiographic contrast as the energy of the incident photons increases and Compton scattering becomes more important.

The photons are typically produced by an x-ray tube running with a voltage between cathode and anode of about 100 kilovolt peak[7] (100 kVp). The anode is usually made

---

[5] Even though the film may have a linear response over a larger range, doubling the exposure usually makes the film too dense to read.

[6] Although a digital detector has greater dynamic range, proper exposure is still important. Too low an exposure introduces noise; an excessive exposure increases he dose to the patient unnecessarily.

[7] The word *peak* is included because the voltage from power supplies in older machines had considerable "ripple" caused by the alternating voltage from the power lines. Even in modern machines, the voltage

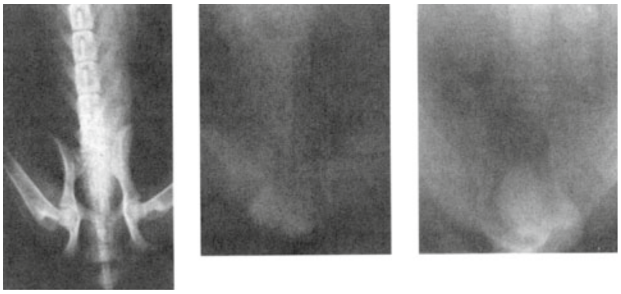

Fig. 16.14 Radiographs taken at 70 kVp, 250 kVp, and 1.25 MeV (^{60}Co), illustrating the loss of contrast for higher energy photons. (From Hendee and Ritenour (2002). Used by permission)

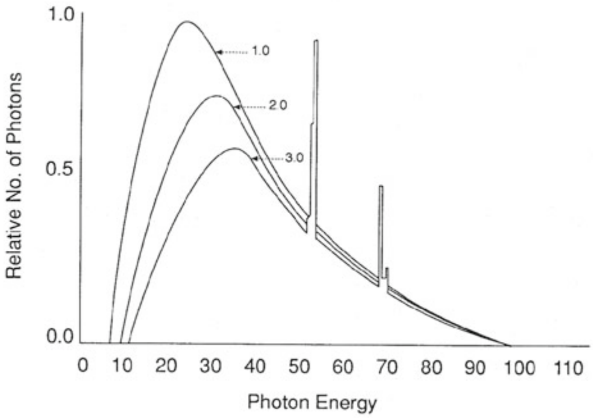

Fig. 16.15 The particle energy spectrum $d\Phi/dE$ from a tube operating at 100 kVp with 1, 2, and 3 mm of aluminum filtration. (From Hendee and Ritenour (2002). Used by permission)

of tungsten (which has a high radiation yield and withstands high temperatures) with a copper backing to conduct thermal energy away. The number of x-rays produced for a given voltage difference depends on the total number of electrons striking the anode, which is proportional to the product of the current and the duration of the exposure (mA s). The anode rotates to help keep it cool. Additional filtration removes low-energy photons that would not get through the body and would not contribute to the image. Figure 16.15 shows the effects of different thicknesses of aluminum on the particle fluence ($d\Phi/dE$) from a tube operating at 100 kVp. The average photon energy depends upon the filtration as well as the kVp, and is about 45 keV for 100 kVp and 2 mm of aluminum filtration (see Problem 18).

16.4.2 Collimation

The collimator is placed just after the x-ray tube. It has adjustable jaws, usually of lead, that limit the size of the beam striking the patient. Making the beam as small as possible reduces the total energy absorbed by the patient. It also reduces the amount of tissue producing Compton-scattered photons that strike the detector and reduce the image quality.

16.4.3 Attenuation in the Patient: Contrast Material

The purpose of a radiograph is to measure features of the internal anatomy of a patient through differences in the attenuation of rays passing through different parts of the body. The photon fluence falls with distance from the x-ray tube as $1/r^2$. It also falls because of attenuation along the path. (We ignore the fact that scattered photons may also strike the detector). We saw in Sect. 15.8 that the mass attenuation coefficient of a compound can be calculated as a weighted average of the elements in the compound:

$$\frac{\mu}{\rho} = \sum_i \left(\frac{\mu}{\rho}\right)_i w_i .$$

Table 16.2 lists various elements, their mass attenuation coefficients at 50 keV, and their composition in water, fat, muscle, and bone. Water and muscle are quite similar, fat has a somewhat smaller attenuation coefficient, and the attenuation of bone is significantly greater.

Figure 16.16 shows attenuation vs. ρx for the beam in Fig. 16.15 with 2 mm of Al filtration in water and in bone. Bone contains calcium, which has a relatively high atomic number, and the attenuation coefficient rises rapidly as the energy decreases. Also shown as dashed lines are the corresponding values of $\exp(-\mu_{\text{atten}} x)$ for the average photon energy in the incident beam, which is 50 keV. In each case the transmitted fraction initially falls more steeply than the dashed line because there is more attenuation of the low-energy photons. For thicker bone the slope of the curve is less than the dashed line because only the high-energy photons remain. This shift of the beam energy and curvature of the attenuation curves is called *beam hardening*.

These differences in attenuation make it easy to distinguish bone from soft tissue. It is also easy to distinguish lungs from other tissues because they contain air and have much lower density. Air-filled lung has a density of 180–320 kg m^{-3}, compared to about 1000 kg m^{-3} for water, muscle, or a solid tumor. Figure 16.17 shows a normal anterior–posterior (A–P) chest radiograph. You can see the exponential decay through layers of bone, the outline of the heart, the arch of the aorta, and the lacy network of

---

pulse applied to the tube may not have a purely rectangular waveform, and kVp may not uniquely determine the x-ray spectrum during the pulse. Modern kilovolt power supplies are described by Sobol (2002).

Table 16.2 Relative composition of various tissues and the attenuation coefficient for 50-keV photons

Element	μ_{atten}/ρ[b] ($\text{m}^2\ \text{kg}^{-1}$)	Fractional mass composition[a]			
		Adipose tissue	Water	Skeletal muscle	Cortical bone, adult
H	0.0336	0.114	0.112	0.102	0.034
C	0.0187	0.598		0.143	0.155
N	0.0198	0.007		0.034	0.042
O	0.0213	0.278	0.888	0.710	0.435
Na	0.0280	0.001		0.001	0.001
Mg	0.0329				0.002
P	0.0492	0.001		0.002	0.103
S	0.0585	0.001		0.003	0.003
Cl	0.0648	0.001		0.001	
K	0.0868			0.004	
Ca	0.1020				0.225
μ_{atten}/ρ ($\text{m}^2\ \text{kg}^{-1}$)		0.0214	0.0227	0.0227	0.0424
ρ (kg m^{-3})		970	1000	1050	1920
μ_{atten} (m^{-1})		20.8	22.7	23.8	81.5

[a] Fractional mass compositions are available at http://physics.nist.gov/PhysRefData/XrayMassCoef/tab2.html

[b] Values are from Hubbell and Seltzer (1996)

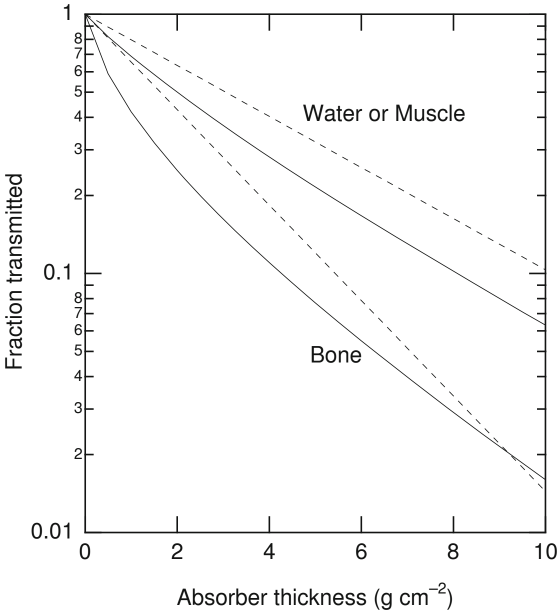

Fig. 16.16 Attenuation of photons in water or muscle and in bone for the spectrum of Fig. 16.15 (100 kVp, 2 mm aluminum filtration). The *dashed lines* are for the attenuation coefficients at 50 keV

blood vessels in the lungs. The patient in Fig. 16.19 has *pneumothorax*. Air has leaked into the pleural cavity and partially collapsed the lungs. You can see this collapse in the upper portion of each lung. Spontaneous pneumothorax can occur in any pulmonary disease that causes an alveolus (air sac) on the surface of the lung to rupture: most commonly emphysema, asthma, or tuberculosis. Pneumothorax can also be caused by perforating trauma to the chest wall. Spontaneous idiopathic (meaning cause unknown) pneumothorax occasionally occurs in relatively young people.

Abdominal structures are more difficult to visualize because except for gas in the intestine, everything has about the same density and atomic number. *Contrast agents* are introduced through the mouth, rectum, urethra, or bloodstream. One might think that the highest-Z materials would be best. However the energy of the K edge rises with increasing Z. If the K edge is above the energy of the x-rays in the beam, then only L absorption with a much lower cross-section takes place. The K edge for iodine is at 33 keV, while that for lead is at 88 keV. Between these two limits (and therefore in the range of x-ray energies usually used for diagnostic purposes), the mass attenuation coefficient of iodine is about twice that of lead. The two most popular contrast agents are barium ($Z = 56$, K edge at 37.4 keV) and iodine ($Z = 53$). Barium is swallowed or introduced into the colon. Iodine forms the basis for contrast agents used to study the cardiovascular system (angiography), gall bladder, brain, kidney, and urinary tract.

If the detector can discriminate photons of different energies, then one can measure photons on either side of an element's K edge, obtaining images that are easily distinguished from the image of background material (Schlomka et al. 2008).

Some pathologic conditions can be identified by the deposition of calcium salts. Such *dystrophic* (defective) calcification occurs in any form of tissue injury, particularly if there has been tissue necrosis (cell death). It is found in necrotizing tumors (particularly carcinomas), atherosclerotic blood vessels, areas of old abscess formation, tuberculous foci, and damaged heart valves, among others.

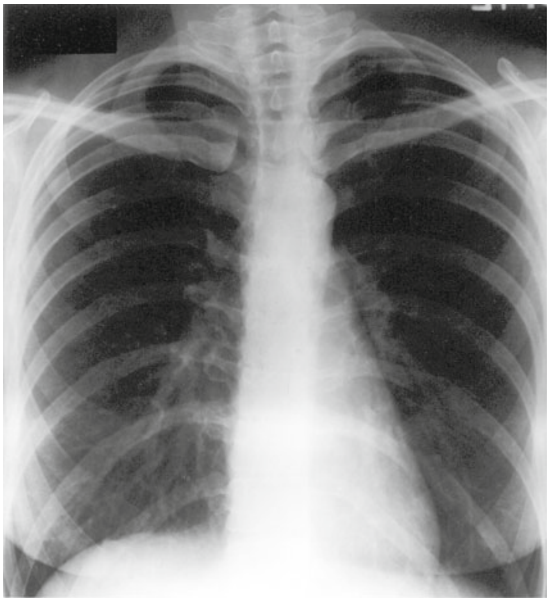

Fig. 16.17 Radiograph of a normal chest. Some of the features are identified in Fig. 16.18 and are described in the text. (Radiograph courtesy of D. Ketcham, M.D., Department of Diagnostic Radiology, University of Minnesota Medical School)

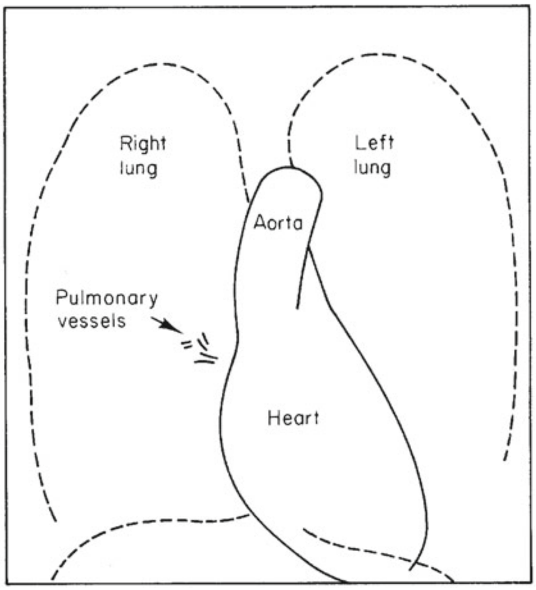

Fig. 16.18 Some of the features in the radiograph of a normal chest, Fig. 16.17

16.4.4 Antiscatter Grid

Since the radiograph assumes that photons either travel in a straight line from the point source in the x-ray tube to the detector or are absorbed, Compton-scattered photons that strike the detector reduce the contrast and contribute an overall background darkening. This effect can be reduced by placing an *antiscatter grid* (or radiographic grid, or "bucky" after its

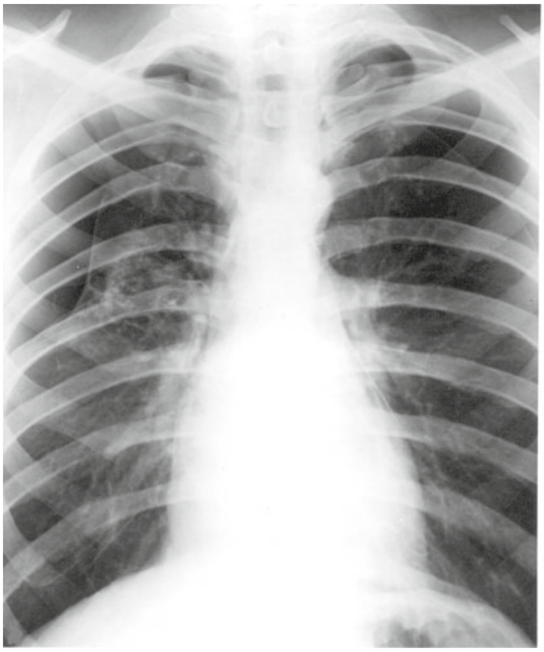

Fig. 16.19 Radiograph of a patient with pneumothorax. Air has escaped from the lungs and caused them to collapse partially. The features are indicated in Fig. 16.20. (Radiograph courtesy of D. Ketcham, M. D., Department of Diagnostic Radiology, University of Minnesota Medical School)

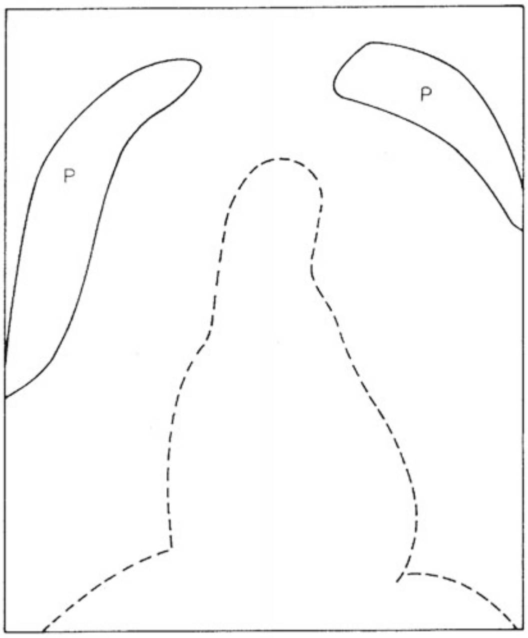

Fig. 16.20 Key to features in Fig. 16.19. The areas of pneumothorax are indicated by *P*. The one on the patient's left (the viewer's right) is difficult to see in the printed version; a radiographic film viewed by transmitted light has a much greater dynamic range

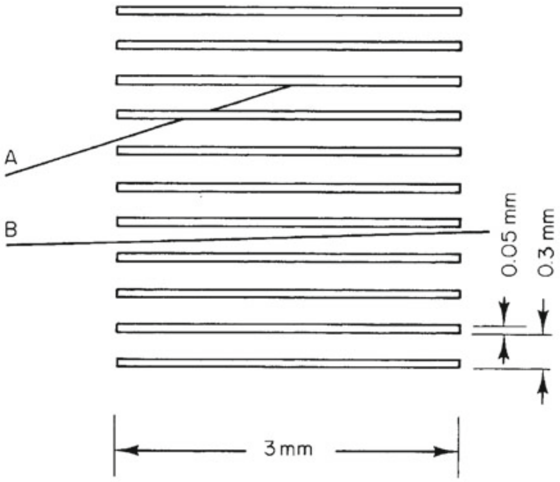

Fig. 16.21 Scale drawing of the elements of a typical grid. The thin lead strips absorb photons that have been scattered through more than a few degrees. As a result background fog due to scattering is reduced and the contrast is increased. Since the x-rays come from a point source, the elements of the grid are usually tilted toward the source and are not parallel over the entire detector surface

inventor, Gustav Bucky) just in front of the detector. Figure 16.21 shows how a grid works. The grid stops x-rays that are not traveling parallel to the sides of the grid strips. A typical grid might have 10–50 strips of lead per centimeter that are 3 mm high and 0.05 mm thick, embedded in plastic or aluminum. The strips can be either parallel or "focused," that is, slanted to aim at the point source on the anode of the x-ray tube. The grid can be either linear or crossed, with strips of lead running in both directions. A grid with a ratio of height to spacing of 12 improves the contrast by a factor of about 3.75, while increasing the exposure to the patient by a factor of about 4.25 to keep the detector dose about the same (Hendee and Ritenour 2002, p. 227). Sometimes the grid is moved during the exposure if the strips in the grid are thick enough to show up on the detector.

16.4.5 Detector

Detectors were described in Sect. 16.3. The film-screen detector is nearly obsolete. In computed radiography a photophosphor or photostimulable phosphor replaces the film-screen combination. The latent image on this phosphor is "read" by a scanning laser beam in a process called photostimulated luminescence. The resulting image is digitized (Rowlands 2002). Direct radiography uses a thin-film transistor detector array (p. 470) to directly produce a digitized image.

16.5 Image Quality

The quality of a radiographic image depends on three things: *resolution*, *contrast*, and *noise*. The resolution and contrast can be described by concepts introduced in Chap. 12 for a linear, shift-invariant system: the point-spread function and its Fourier transform, the optical transfer function, whose magnitude is the modulation transfer function.[8] The noise arises primarily from the fluctuations in the number of photons striking a given area of the detector—quantum noise—though granularity of the film or detector array is also important.

The transfer function for the entire system depends on many factors: the tube and spot size, filter, source–screen and source–patient distances, grid, detector, and scatter. If each of these subsystems operates in series, as in an audio system, one can successively convolve the point-spread functions or multiply together the (complex) optical transfer functions. It is also possible to have parallel[9] subsystems, each contributing to the final image, in which case the analysis is more complicated. An excellent review of the use of transfer-function analysis in radiographic imaging is the article by Metz and Doi (1979). The text by Macovski (1983) is at about the level of this book and presents many details of noise and convolution for radiographic, fluoroscopic, tomographic, nuclear medicine, and ultrasound images. The size of the spot where the electrons strike the anode of the x-ray tube is critical in determining the resolution of the final image, as discussed in detail by Wagner et al. (1974).

The *exposure contrast* is the change in exposure between two (usually adjacent) parts of the image divided by the average:

$$C_{\mathrm{in}} = \frac{\Delta X}{X}. \tag{16.13}$$

This is similar to the modulation defined in Eq. 12.20. The *brightness contrast* is the analogous quantity for the light from the computer display or the light transmitted through the processed film:

$$C_{\mathrm{out}} = \frac{\Delta T}{T}. \tag{16.14}$$

---

[8] The point-spread function of a detector is easily measured. A point source is created by passing the x-rays through a pinhole in a piece of lead placed directly on the detector. The resulting image is the point-spread function. We saw in Chap. 12 how this is related to the modulation transfer function. Standard techniques have been developed for measuring the modulation transfer function (MTF) (ICRU Report 41 1986; ICRU Report 54 1996).

[9] Examples of parallel subsystems are the two emulsion layers on double-coated film, and the effect of primary and scattered radiation on the formation of the image.

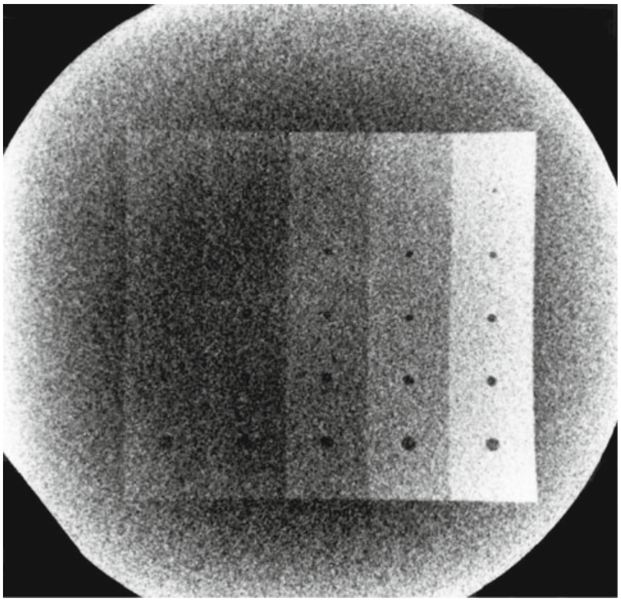

Fig. 16.22 An example of the relationship among exposure, image size, and detectability. A type 1100 aluminum phantom was imaged with digital fluorography. It was exposed to an 80-kVp x-ray beam with 4.5-mm Al filter. As the image becomes lighter, the thickness of the aluminum phantom increases in steps: 0.85, 1.3, 2.1, 3.2, and 5.2 mm. The holes are 1, 1.5, 2, 2.5, and 3 mm in diameter. As the attenuation in the aluminum increases, so does the signal, and the easier it is to detect the smaller holes. (Photograph courtesy of Richard Geise, Ph.D., Department of Radiology, University of Minnesota)

The exposure contrast and brightness contrast are proportional (Eq. 16.11):

$$C_{\text{out}} = \gamma C_{\text{in}}. \tag{16.15}$$

The *radiographic signal* is a small change in optical brightness in adjacent areas of the image. Changes in brightness below a certain value are not detectable by the viewer. This is apparent in Fig. 16.22, which shows signals with different contrasts and different sizes on a uniform background. The smaller the diameter of the signal region, the more difficult the signal is to detect. We will develop a simple model to explain why.

Suppose first that there is no signal, but that the detector is illuminated with a uniform beam of x-rays with a constant fluence. We make an exposure for a certain time and count the number of photons striking a sampling area of the detector, S. Though the average fluence is constant across the detector, the photons are randomly distributed. A somewhat different number of photons strike a nearby sampling area of the same size. This is a situation where the average number striking a sampling area of a given size is constant, the total number of photons is very large, and the probability that any one photon is absorbed in a given sampling area is small, so the situation is described by Poisson statistics (Appendix J). The mean number of photons striking a sampling area is ΦS and the standard deviation is $(\Phi S)^{1/2}$. Suppose that some fraction $f \le 1$ of these photons actually interact with the detector. Then the mean number interacting is $f\Phi S$ and the standard deviation is[10] $(f\Phi S)^{1/2}$. Thus there are fluctuations in the brightness of the image across the uniformly exposed viewing region, just because of the Poisson statistics—quantum noise or shot noise—of the x-ray photons striking the detector.

The fluctuations in the number of photons striking area S can be related to fluctuations in the exposure of that area of the detector, and hence to the response of the detector. Since the exposure (measured in air just in front of the detector) is proportional to the photon fluence, $X = A\Phi$, $\overline{(X-\overline{X})^2} = A^2\overline{(\Phi-\overline{\Phi})^2}$ and $(\Delta X)_{\text{rms}} = A(\Delta\Phi)_{\text{rms}}$. We define the *noise exposure contrast* to be the standard deviation of the number of photons affecting the detector in area S divided by the average number affecting an area that size:[11]

$$C_{\text{noise in}} \equiv \frac{(f\Phi S)^{1/2}}{f\Phi S} = (f\Phi S)^{-1/2}. \tag{16.16}$$

The *noise brightness contrast* is then

$$C_{\text{noise out}} = \gamma (f\Phi S)^{-1/2}. \tag{16.17}$$

The fluctuations in the noise, measured by noise contrast, are inversely proportional to the square root of the area of the lesion to be detected.[12] This is seen in Fig. 16.22. The noise in the system is determined by measuring the charge collected in each pixel of the uniformly exposed detector. Variations with position can be described either in terms of its two-dimensional autocorrelation function or its Fourier transform, the *Wiener spectrum*. The radiographic noise consists of three components: *quantum mottle*, the statistical fluctuations in the number of photons absorbed in a small area (shot noise); *structure mottle* due to nonuniformities in the x-ray absorbing layer of the detector, and *graininess*, variation in the size and distribution of the transistors in the detector. Here we discuss only quantum mottle.

---

[10] This is very similar to the arguments about the fraction of photons absorbed by a visual pigment molecule in Eq. 14.68. Changes in the value of f in Fig. 14.43 shift the response curve along the axis.

[11] It is sometimes useful to write it as

$$C_{\text{noise in}} \equiv \frac{(f\Phi S)^{1/2}}{f\Phi S} = \frac{1}{f^{1/2}S^{1/2}}\frac{(\Delta\Phi)_{\text{rms}}}{\Phi} = \frac{1}{f^{1/2}S^{1/2}}\frac{A(\Delta X)_{\text{rms}}}{AX}$$
$$= \frac{1}{f^{1/2}S^{1/2}}\frac{(\Delta X)_{\text{rms}}}{X}.$$

[12] An analogous phenomenon is seen when counting individual photons with a radiation detector at a fixed average rate. The number counted in a given time interval fluctuates, with the fractional fluctuation inversely proportional to the square root of the counting time.

Now introduce a signal, which is a small increase in the exposure or photon fluence: $\Delta X_{\text{signal}} = A\Delta\Phi_{\text{signal}}$. This gives a brightness contrast

$$C_{\text{signal out}} = \gamma \frac{\Delta X_{\text{signal}}}{X} = \gamma \frac{\Delta\Phi_{\text{signal}}}{\Phi}. \tag{16.18}$$

The ratio of the signal contrast to the noise contrast is called the *signal-to-noise ratio*:

$$\text{SNR} = \frac{C_{\text{signal out}}}{C_{\text{noise out}}} = \frac{\gamma\left(\Delta\Phi_{\text{signal}}/\Phi\right)}{\gamma\left(f\Phi S\right)^{-1/2}} = (fS)^{1/2}\frac{\Delta\Phi_{\text{signal}}}{\Phi^{1/2}}. \tag{16.19}$$

The signal will be detectable only if the signal brightness contrast exceeds the noise brightness contrast by a certain amount:[13]

$$\text{SNR} > k, \qquad (fS)^{1/2}\frac{\Delta\Phi_{\text{signal}}}{\Phi^{1/2}} > k. \tag{16.20}$$

The larger the value of the signal-to-noise ratio, the greater the probability of detecting the signal. Many experiments on detecting lesions in a noisy background have been done; they will not be discussed here.[14] Values of k that are used range from 2 to 5.

Let us apply the result in Eq. 16.20 to a simple model: a monoenergetic x-ray beam passing through a patient. The total thickness of the patient is L. The attenuation coefficient is μ. If an x-ray beam with fluence Φ_0 strikes the patient, the fluence of x-ray photons emerging is $\Phi_1 = \Phi_0 e^{-\mu L}$. Imagine a nearby region where for a distance x the attenuation coefficient is $\mu - \Delta\mu$. The x-ray fluence emerging along a line passing through this region is

$$\begin{aligned}\Phi_2 &= \Phi_0 e^{-\mu(L-x)-(\mu-\Delta\mu)x} = \Phi_0 e^{-\mu L} e^{\Delta\mu x}\\ &= \Phi_1 e^{\Delta\mu x}\\ &\approx \Phi_1(1 + x\,\Delta\mu).\end{aligned} \tag{16.21}$$

The exposure contrast is therefore $C_{\text{in}} = (\Delta\Phi)_{\text{signal}}/\Phi_1 \approx x\,\Delta\mu$. We combine this with Eq. 16.20 to obtain

$$(fS\Phi_1)^{1/2}(x\,\Delta\mu) > k, \tag{16.22}$$

where Φ_1 is the fluence leaving the patient or striking the detector. (These are the same if variations in $1/r^2$ can be neglected, where r is the distance from the tube to the patient or the tube to the detector). The signal-to-noise ratio increases as the square root of the photon fluence or exposure, the square root of the area to be detected, and the square root of f, the fraction of the photons striking the detector that are actually detected.

The fraction f in this Poisson model is equal to the *detective quantum efficiency* (DQE). It is easily visualized as the fraction of the photons striking the detector that actually affect it. The number of *noise equivalent quanta* (NEQ) in our model is $f\Phi_1$.[15]

We can apply Eq. 16.22 to determine the number of photons that must be transmitted through the patient for a given image size and given signal-to-noise ratio. We assume that $f = 1$. The required photon fluence emerging from the patient is (dropping the subscript on Φ_1)

$$\Phi S > \left(\frac{k}{x\,\Delta\mu}\right)^2. \tag{16.23}$$

If the lesion thickness is $x = 1$ cm and $\Delta\mu = 0.01\mu_{\text{water}} = (0.01)(22.7)\ \text{m}^{-1}$, then $x\,\Delta\mu = 0.00227$. For $k = 4$, the number of photons in the image area must be greater than 3×10^6. The exit dose to the patient is (assuming monoenergetic photons)

$$\begin{aligned}D_{\text{body}} &= \Psi\left(\frac{\mu_{\text{en}}}{\rho}\right)_{\text{body}} = (h\nu)\Phi\left(\frac{\mu_{\text{en}}}{\rho}\right)_{\text{body}}\\ &= \frac{(h\nu)(3\times 10^6)}{S}\left(\frac{\mu_{\text{en}}}{\rho}\right)_{\text{body}}.\end{aligned} \tag{16.24}$$

The dose increases as the area to be detected decreases. In order to detect an image 1 mm square using 50-keV photons, the exit dose in water would have to be at least 9.8×10^{-5} Gy.

16.6 Angiography and Digital Subtraction Angiography

One important problem in diagnostic radiology is to image portions of the vascular tree. *Angiography* can confirm the existence of and locate narrowing (stenosis), weakening and bulging of the vessel wall (aneurysm), congenital malformations of vessels, and the like. This is done by injecting

---

[13] There are statistical fluctuations in the signal as well as the noise. The variance of the difference between signal and noise will be the sum of the variances in the signal and in the noise. This has the effect of increasing the noise by a factor of $\sqrt{2}$, which can be absorbed in the value of k that is chosen. See Problem 23.

[14] The ability to detect the signal accurately is greater when the observer knows the nature of the signal and is only asked whether it is or is not present. That is, the ability of an observer to detect a signal is less in the more realistic situation where the observer does not know what the signal is or where it might be in the radiograph.

[15] This simple equality exists only because we are using a model with Poisson statistics. The DQE is defined more generally as the square of the signal-to-noise ratio of the detector output divided by the square of the signal-to-noise ratio of the detector input. The more general definitions of DQE and NEQ are discussed in Wagner (1983) and Wagner (1977).

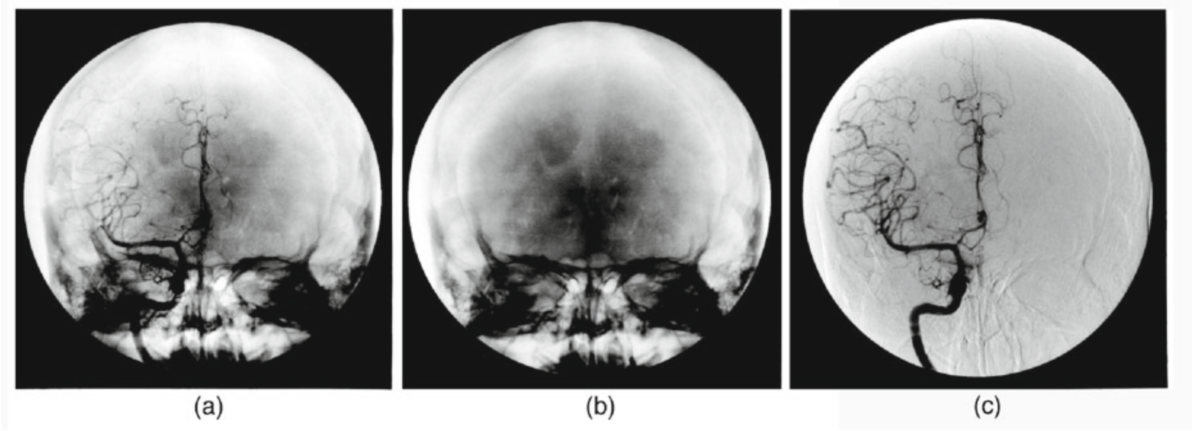

Fig. 16.23 Digital subtraction angiography. **a** Brain image with contrast material. **b** Image without contrast material. **c** The difference image. Anterior view of the right internal carotid artery. (Photograph courtesy of Richard Geise, Ph.D., Department of Radiology, University of Minnesota)

a contrast material containing iodine into an artery. If the images are recorded digitally, it is possible to subtract one without the contrast medium from one with contrast and see the vessels more clearly (Fig. 16.23).

In a typical angiographic study, 30–50 ml of contrast material is injected into an artery. For a vessel with a diameter of 8 mm, ρx of the contrast material is about 4 mg cm^{-2}.

16.7 Mammography

Mammography poses particular challenges for medical physicists. The resolution needed is extremely high (about 15 line pairs (lp) mm^{-1} compared to 5 lp mm^{-1} for a chest radiograph).[16] The radiologist may use a magnifying glass to inspect the image. The contrast in a breast image is inherently low. Fat and glandular tissue must be distinguished by the slight differences in their attenuation coefficients (see Problem 25). The dose must be made as small as possible.

These challenges have been met. Spatial frequencies of 14–16 lp mm^{-1} are routinely obtained. Noise limits the minimum size of a detectable object to $>$ 0.3 mm for microcalcifications or a few millimeters for soft tissue. Digital mammography is providing even higher resolution (Pisano and Yaffe 2005). The typical mammographic dose per view has been reduced from about 50 mGy in the 1960s and 4.1 mGy in the 1970s to 0.4 mGy in 2008.[17] One technique that has led to these improvements is the molybdenum target x-ray tube, operating at 25–28 kVp. Figure 16.24 shows the photon fluence from such a tube, with the 17-keV K_α and 19-keV K_β lines being quite prominent. Filtration of the beam with the same material, molybdenum, further sharpens the spectrum. The K edge of molybdenum occurs at an energy just above the K_β line, removing photons for energies over about 20 keV. The dashed lines show the spectrum when a molybdenum filter is used. These photons interact primarily by the photoelectric effect, so attenuation depends strongly on atomic number. There are few Compton-scattered photons to degrade the image.

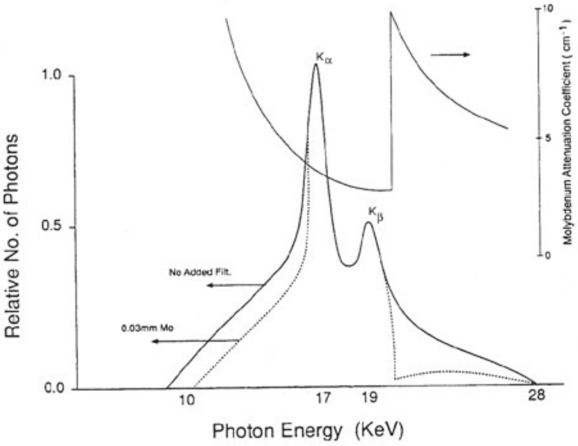

Fig. 16.24 The x-ray spectrum from a molybdenum anode tube used for mammography, with and without filtration by a molybdenum foil. (From Hendee and Ritenour 2002. Used by permission)

16.8 Computed Tomography

Radiographs provide only an integrated value of the attenuation coefficient. That is, if $N_0(y,z)$ monoenergetic x-ray photons traverse the body along a line in the x direction after

---

[16] Line pairs (abbreviated lp) are analogous to the period of a square wave.

[17] See NCRP Report 100 (1989) for early data; Mettler et al. (2008) for 2008 data.

entering the body at coordinates (y, z), the number emerging without interaction is $N(y, z) = N_0(y, z)e^{-\alpha(y,z)}$, where

$$\alpha(y, z) = \int \mu(x, y, z)\, dx.$$

The radiograph measures $N(y, z)$ or $\alpha(y, z)$. The desired information is $\mu(x, y, z)$. The radiographic image is often difficult to interpret because of this integration along x. For example, it may be difficult to visualize the kidneys because of the overlying intestines.

Several types of computed tomography (*tomos* means slice) have been developed in the last few decades. They include *transmission computed tomography* (CT), *single-photon emission computed tomography* (SPECT), and *positron emission tomography* (PET). They all involve reconstructing, for fixed z, a map of some function $f(x, y)$ from a set of projections $F(\theta, x)$, as described in Sect. 12.4 and 12.5. For CT the function f is the attenuation coefficient $\mu(x, y)$. For SPECT and PET it is the concentration of a radioactive tracer within the body, as will be described in Chap. 17.

The history of the development of computed tomography is quite interesting (Kalender 2011). The Nobel Prize in Physiology or Medicine was shared in 1979 by a physicist, Allan Cormack, and an engineer, Godfrey Hounsfield. Cormack had developed a theory for reconstruction and done experiments with a cylindrically symmetric object that were described in two papers in the *Journal of Applied Physics* in 1963 and 1964. Hounsfield, working independently, built the first clinical machine, which was installed in 1971. It was described in 1973 in the *British Journal of Radiology*. The Nobel Prize acceptance speeches (Cormack 1980; Hounsfield 1980) are interesting to read. A neurologist, William Oldendorf, had been working independently on the problem but did not share in the Nobel Prize (See DiChiro and Brooks 1979; and Broad 1980).

Early machines had an x-ray tube and detector that moved in precise alignment on opposite sides of the patient to make each pass. The size of these machines allowed only heads to be scanned. After one pass, the gantry containing the tube and detector was rotated 1 ° and the next pass was taken. After data for 180 passes were recorded, the image was reconstructed. A complete scan took about 4 min.

Figure 16.25 shows the evolution of the detector and source configurations. The third generation configuration is the most popular. All of the electrical connections are made through slip rings. This allows continuous rotation of the gantry and scanning in a spiral as the patient moves through the machine. Interpolation in the direction of the axis of rotation (the z axis) is used to perform the reconstruction for a particular value of z. This is called *spiral CT* or *helical CT*. Kalender (2011) discusses the physical performance of CT machines, particularly the various forms of spiral machines. There may be a single row of detectors or multiple detector rows parallel to the z axis. Table 16.3 shows how scanners have improved since they were first introduced. Spiral CT provides $\mu(x, y, z)$, and the images can be displayed in three dimensions.

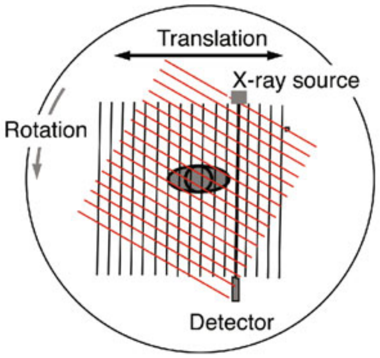

(a) First Generation: Translation and Rotation

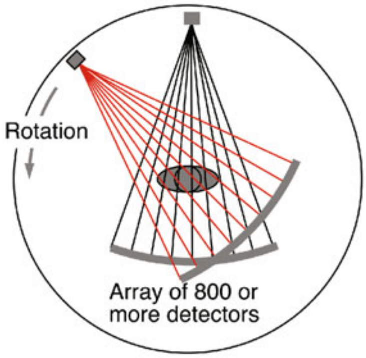

(b) Third Generation: Rotation

Fig. 16.25 Scanning techniques used in CT scanners. **a** In the earliest scanners the x-ray tube and detector moved in synchronization on either side of the subject. Then their translation path was rotated one degree. **b** Nearly all machines now use the "third generation" configuration: a fan beam and multidetector array rotate continuously around the patient

Figure 16.26 is an abdominal scan showing a benign tumor in the liver. Computer analysis of $\mu(x, y, z)$ data can be used to display 3-dimensional images of an organ (Fig. 16.27). The surface of an organ is defined by a change in μ.

It is often desirable to measure the attenuation coefficient with an accuracy of $\pm 0.5\,\%$. For water at 60 keV, $\mu = 20\ \mathrm{m}^{-1}$, so μ must be measured with an accuracy of $\delta\mu = 0.1\ \mathrm{m}^{-1}$. (A beam of 120 kVp with 2–3 mm of aluminum filtration has about this average photon energy). It is customary to report the fractional difference between μ and μ_{water}. The *Hounsfield unit* is

$$H = 1000 \frac{\mu_{\mathrm{tissue}} - \mu_{\mathrm{water}}}{\mu_{\mathrm{water}}}. \tag{16.25}$$

The desired accuracy is ±5 Hounsfield units.

Table 16.3 The evolution of typical values for high-performance CT machines. (Adapted from Kalender 2011, p. 41)

Feature	1972	1980	1990	2000	2010
Minimum scan time	300 s	5–10 s	1–2 s	0.33–0.5 s	0.27–0.35 s
Data per 360 ° scan	57.6 kB	0.2–1 MB	1–2 MB	5–20 MB	0.1–1 GB
Data per spiral scan			12–24 MB	0.1–1 GB	1–100 GB
Image matrix	80 × 80	256 × 256	512 × 512	512 × 512	512 × 512
Power (kW)	2	10	40	60–100	80–120
Slice thickness (mm)	13	2–10	1–10	0.5–1	0.4–0.6
Spatial resolution (Line pair cm^{-1})	3	8–12	10–15	12–16	12–25

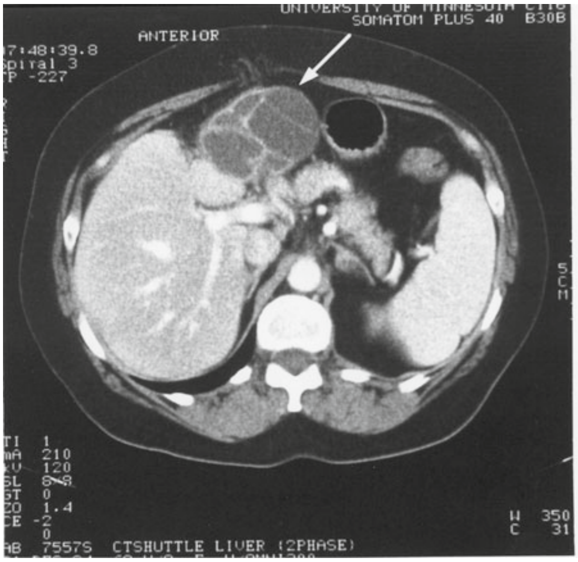

Fig. 16.26 A spiral CT scan of the abdomen. The arrow points to a biliary cystadenoma, a benign tumor of the liver. (Scan courtesy of E. Russell Ritenour, Ph.D., Department of Radiology, University of Minnesota Medical School)

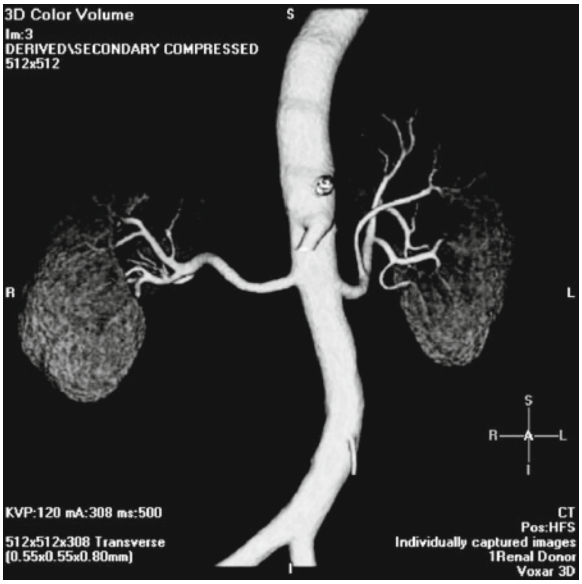

Fig. 16.27 A 3-dimensional rendering of the aorta, renal arteries and kidneys. (Scan courtesy of E. Russell Ritenour, Ph.D., Department of Radiology, University of Minnesota Medical School)

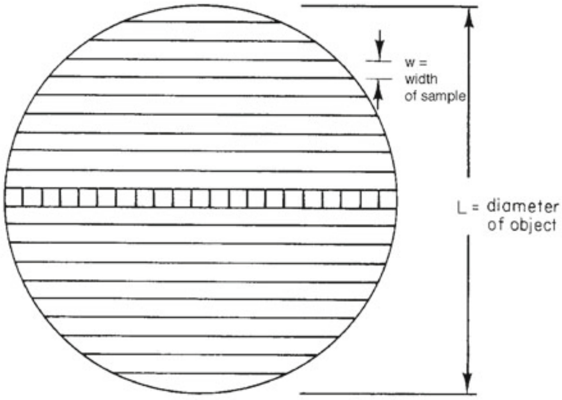

Fig. 16.28 A circular object that is to be analyzed. The diameter of the object is L; the width of each sample in the scan is w. It is desired to resolve voxels in each sample which have a length w on each side, as shown for the center diameter

There is a fundamental relationship between the dose to the patient and the resolution. We derive it here for a first-generation machine. Suppose we are reconstructing the image of an object with a circular cross-section as shown in Fig. 16.28. The object is to be resolved into cubic volume elements or *voxels* of length w on each side parallel to the x, y and z axes. The length of each voxel along the z axis perpendicular to the scan is the slice thickness. The diameter of the object is L. For simplicity, we make the analysis assuming a first-generation machine, with rectilinear passes repeated at m different angles between 0 and 180 °. The width of each sample in a scanner pass is w. The number of samples in each pass is

$$n = \frac{L}{w}, \tag{16.26}$$

and the number of voxels in the object is approximately the area of the circular object divided by the area of the voxel in the plane of the slice: $\pi L^2/4w^2$ or $\pi n^2/4$. To determine $\pi n^2/4$ independent values of μ requires at least that many independent measurements. Since n measurements are made in each pass, we need m passes where $mn = \pi n^2/4$ or

$$m = \frac{\pi n}{4}. \tag{16.27}$$

With more passes the situation is overdetermined; with fewer it is underdetermined. If the values of μ are overdetermined, convolved back projection (Chap. 12) or a similar procedure can be used to assign the values of μ.

Now consider the attenuation of photons along a diameter of the object in one pass. In Sect. 16.5 we developed a relationship between the photon fluence in the beam needed to measure the attenuation with some desired accuracy (Eq. 16.21). The same arguments can be applied in this case:

$$\delta\Phi = \Phi_1 w\,\delta\mu .$$

The photons arrive at the detector, which we assume for simplicity to have 100 % efficiency, at a constant average rate, so they are Poisson distributed. The standard deviation in the number of counts is $(\Phi_1 S)^{1/2} = (\Phi_1 w^2)^{1/2}$. To detect the difference between the two samples, $w^2\delta\Phi$ must exceed this by the minimum signal-to-noise ratio, k. This gives the minimum photon fluence at the detector:

$$\Phi_1 > \frac{k^2}{w^4(\delta\mu)^2}. \qquad (16.28)$$

It can be shown (Brooks and DiChiro 1976a) that these counts can be divided among all the passes. Since the dose is proportional to Φ_1, this equation shows a fundamental relationship between dose and resolution. Decreasing w by a factor of 2 requires a 16-fold increase in dose, while improving $\delta\mu$ by a factor of 2 requires a dose that is 4 times as large. For further discussion of this equation, see Kalender (2011) pp. 169–170. We discuss CT dose in Sect. 16.12. Reducing the dose is a matter of great current interest (Tack and Gevenois 2007).

16.9 Biological Effects of Radiation

Radiation at sufficiently high doses can kill cells, tumors, organs, or entire animals. Radiation, along with surgery and chemotherapy, is a mainstay of cancer treatment. Radiation can also cause mutations. *Radiobiology*, the study of how radiation affects cells and organs, has provided major improvements in our understanding of cell death and damage. This understanding has modified and improved our approach to radiation therapy. This section provides a brief introduction to radiobiology, but it ignores many important details. For these details see Hall and Giaccia (2012). The discussion starts with some cell-culture (*in vitro*) results, presents the most frequently used model for radiation damage, and then moves to *in vivo* tissue irradiation and the eradication of tumors.

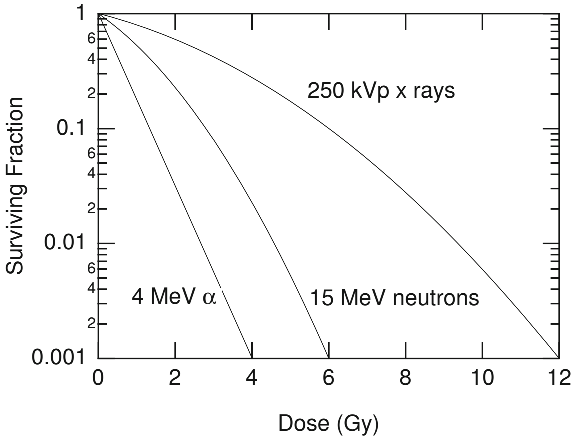

Fig. 16.29 Typical survival curves for cell culture experiments, for 4-MeV α particles, 15-MeV neutrons, and 250-kVp x-rays. These are representations of typical experimental data

There are two types of effects. *Deterministic* or *tissue reactions* occur immediately (early effects) and include skin reddening (erythema) and cataracts. Late effects are stochastic and include cancer and mental retardation for fetal irradiation exceeding 0.3 Gy. We discuss only stochastic effects here.

16.9.1 Cell-Culture Experiments

Cell-culture studies are the simplest conceptually. A known number of cells are harvested from a stock culture and placed on nutrient medium in plastic dishes. The dishes are then irradiated with a variety of doses including zero as a control. After a fixed incubation period the cells that survived irradiation have grown into visible colonies that are stained and counted. Measurements for many absorbed doses give *survival curves* such as those in Fig. 16.29. These curves are difficult to measure for more than two or three decades, because of the small number of colonies that remain.

Failure to survive means either that the cell was killed or that it can no longer reproduce. If the cells die attempting the next or a later cell division (*mitosis*) it is called *mitotic death*. Some cells die by *apoptosis:* a mechanism whereby the cell initiates its own programmed death, going through a well-defined series of morphologic events that culminate in fragmentation of the DNA (Hall and Giaccia 2012). Experiments with microscopic beams of radiation and short-range particles aimed at different parts of the cell have demonstrated that damage to the cell's DNA is only one factor in the cell's response to the radiation. Nonetheless, the differences in survival curve shapes that we discuss here are still important.

The shape of the survival curve depends on the linear energy transfer (LET) of the charged particles. For the α particles in Fig. 16.29 the LET is about 160 keV μm^{-1}, for neutrons it is about 12 keV μm^{-1}, and for the electrons from the 250-kVp x-rays it is about 2 keV μm^{-1}. The α particles and neutrons are called high-LET radiation; the electrons are low-LET radiation.

High-LET radiation produces so many ion pairs along its path that it exerts a direct action on the cellular DNA. Low-LET radiation can also ionize, but it usually acts indirectly. It ionizes water (primarily) according to the chemical reaction

$$\mathrm{H_2O} \rightarrow \mathrm{H_2O^+} + e^-.$$

The $\mathrm{H_2O^+}$ ion decays with a lifetime of about 10^{-10} s to the hydroxyl free radical:

$$\mathrm{H_2O^+} + \mathrm{H_2O} \rightarrow \mathrm{H_3O^+} + \mathrm{OH}.$$

This then produces hydrogen peroxide and other free radicals that cause the damage by disrupting chemical bonds in the DNA.

16.9.2 Chromosome Damage

Cellular DNA is organized into *chromosomes*. In order to understand radiation damage to DNA, we must recognize that there are four *phases* in the cell division cycle:

M	Cell division. This stage includes both division of the nucleus (*mitosis*) and of the cytoplasm (*cytokinesis*). This phase may last 1 or 2 h.
G_1	The first "gap" phase. The cell is synthesizing many proteins. The duration of G_1 determines how frequently the cells divide. It varies widely by kind of tissue, from a few hours to 200 h.
S	Synthesis. A new copy of all the DNA is being made. This lasts about 8 h.
G_2	The second "gap" phase, lasting about 4 h.

Figure 16.30 shows, at different magnifications, a strand of DNA, various intermediate structures that we will not discuss, and a chromosome as seen during the M phase of the cell cycle. The size goes from 2 nm for the DNA double helix to 1400 nm for the chromosome. In addition to cell survival curves one can directly measure chromosome damage. There is strong evidence that radiation, directly or indirectly, breaks a DNA strand. If only one strand is broken, there are efficient mechanisms that repair it over the course of a few hours using the other strand as a template. If both strands are broken, permanent damage results, and the next cell division produces an abnormal chromosome.[18] Several forms of abnormal chromosomes are known, depending on where along the strand the damage occurred and how the damaged pieces connected or failed to connect to other chromosome fragments. Many of these chromosomal abnormalities are lethal: the cell either fails to complete its next mitosis, or it fails within the next few divisions. Other abnormalities allow the cell to continue to divide, but they may contribute to a multistep process that sometimes leads to cancer many cell generations later.

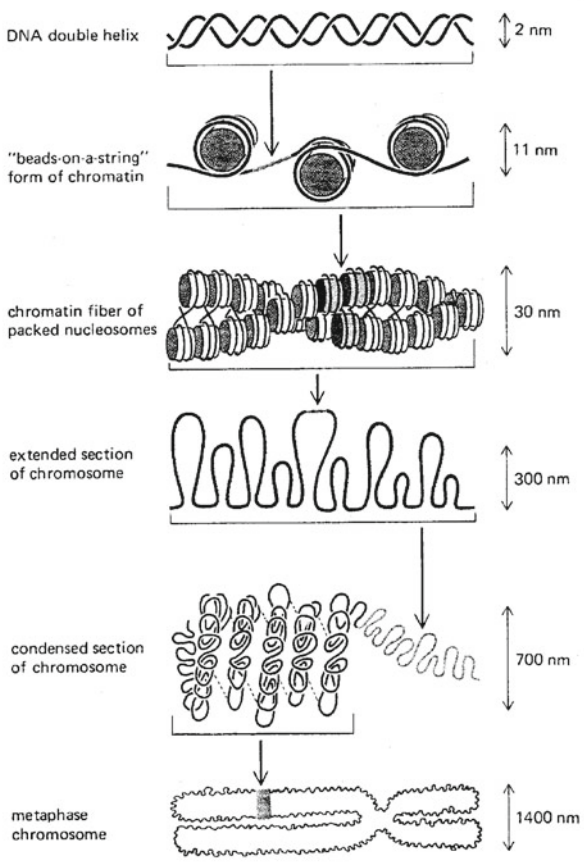

Fig. 16.30 A schematic diagram of how the DNA is packed to give a chromosome, shown at metaphase of the cell cycle. (Republished with permission of Taylor and Francis Group from Alberts et al. (1999, p. 230). Permission conveyed through Copyright Clearance Center, Inc)

Even though radiation damage can occur at any time in the cell cycle (albeit with different sensitivity),[19] one looks for chromosome damage during the next M phase, when the

---

[18] This is a simplification. It is possible for a double strand break to repair properly. See Hall and Giaccia (2012, p. 18).

[19] In general, cells exhibit the greatest sensitivity in M and G_2.

DNA is in the form of visible chromosomes as in the bottom example in Fig. 16.30. If the broken fragments have rejoined in the original configuration, no abnormality is seen when the chromosomes are examined. If the fragments fail to join, the chromosome has a "deletion." If the broken ends rejoin other broken ends, the chromosome appears grossly distorted.

A sequence of processes leads to cellular inactivation. Ionization is followed by initial DNA damage. Most of this is repaired, but it can be repaired incorrectly. No repair or faulty repair results in DNA lesions that are then manifest as chromosome aberrations, which may be nonlethal, may cause mutations, or may lead to cell death. The numbers quoted here are from the review by Steel (1996). A cell dose of 1 Gy leads to the production of about 2×10^5 ion pairs per cell nucleus, of which about 2000 are produced in the cell's DNA. It has been estimated that the amount of DNA damage immediately after radiation can be quite large: 1000 single-strand breaks and 40 double-strand breaks per Gy. Yet survival curves for different cell types show between 0.3 and 10 lethal lesions per gray of absorbed dose. Thus the amount of repair that takes place is quite large, and the model introduced below is an oversimplification.

A number of chemicals enhance or inhibit the radiation damage. Some chemical reactions can "fix" (render permanent) the DNA damage, making it irreparable; others can scavenge and deactivate free radicals. One of the most important chemicals is oxygen, which promotes the formation of free radicals and hence cell damage. Cells with a poor oxygen supply are more resistant to radiation than those with a normal supply.

16.9.3 The Linear-Quadratic Model

The *linear-quadratic model* is often used to describe cell survival curves. We will extended it to very small survival rates that cannot possibly be confirmed experimentally. We use it as a simplified model for DNA damage from ionizing radiation that recognizes two types of damage, shown in Fig. 16.31. In type-A damage a single ionizing particle breaks both strands of the DNA, and the chromosome is broken into two fragments. In type-B damage, a single particle breaks only one strand. If another particle breaks the other strand "close enough" to the first break before repair has taken place, then the chromosome suffers a complete break.

The probability of type-A damage is proportional to the dose. The average number of cells with type-A damage after dose D is $m = \alpha D = D/D_0$, and the probability of no damage is the Poisson probability $P(0; m) = e^{-m} = e^{-\alpha D}$. This is the dashed line in Fig. 16.32, which is redrawn from Fig. 16.29. For radiations with higher LET the proportionality constant is greater, as seen in Fig. 16.29.

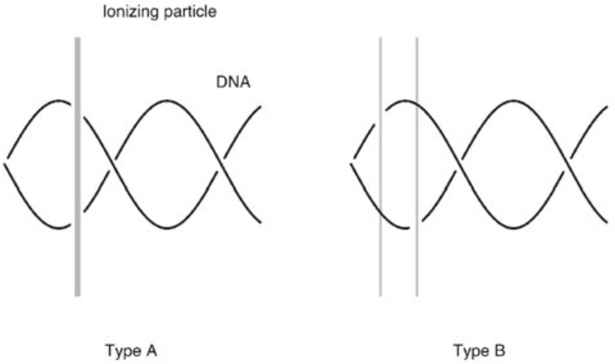

Fig. 16.31 The two postulated types of DNA damage from ionizing radiation for our simple model to explain the linear-quadratic cell culture survival curve. In type-A damage a single ionizing particle breaks both strands. Two ionizing particles are required for type-B damage, one breaking each strand

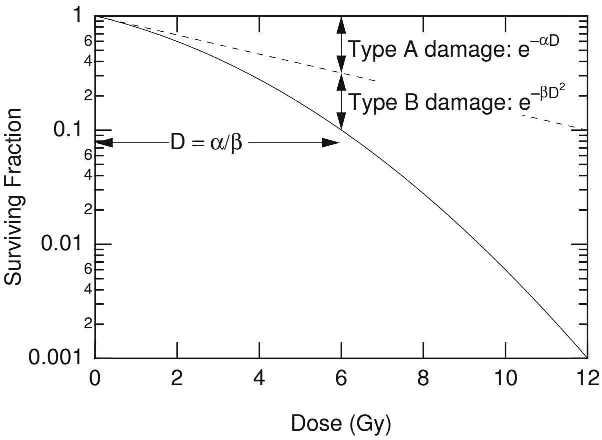

Fig. 16.32 A survival curve, showing the linear exponent for type-A damage and the quadratic exponent for type-B damage

In type-B damage one strand is damaged by one ionizing particle and the other by another ionizing particle. The probability of fragmenting the DNA molecule is therefore proportional to the square of the dose. The average number of molecules with type-B damage is βD^2, and the survival curve for type-B damage alone is $e^{-\beta D^2}$, also shown in Fig. 16.32. This leads to the linear-quadratic model for cell survival:

$$P_{\text{survival}} = e^{-\alpha D - \beta D^2}. \tag{16.29}$$

The dose at which mortality from each mechanism is the same is α/β, as shown in Fig. 16.32.

An extension of the cell survival experiments is the *fractionation curve* shown in Fig. 16.33. After a given dose, cells from the culture were harvested and used to inoculate new cultures. After a few hours they were irradiated again. The survival curve plotted against total dose starts anew from the

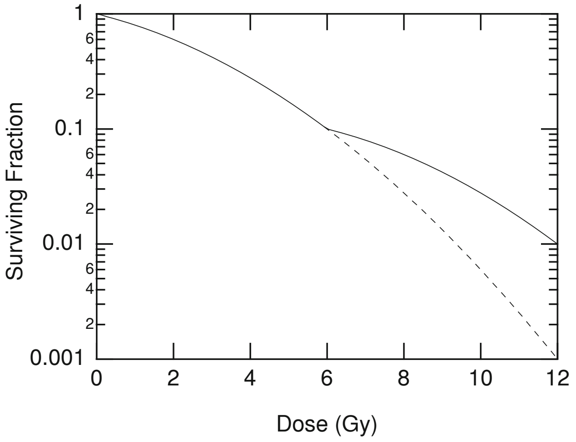

Fig. 16.33 If the dose for low-LET radiations is divided into fractions, with a few hours between fractions, all of the single-strand breaks have been repaired, and survival follows the same curve as for the original fraction

point corresponding to the first irradiation. The initial dose of 6 Gy caused both type-A and type-B damage. Before the second dose, the cells with single-strand damage had been repaired, and when the second dose was given, it acted on undamaged cells, so that only type-A damage occurred for small additional doses.

16.9.4 The Bystander Effect

Ionization damage is not the entire story. The *bystander effect* in radiobiology refers to the "induction of biological effects in cells that are not directly traversed by a charged particle, but are in close proximity to cells that are" (Hall 2003; Hall and Giaccia 2012).

One experiment showing the bystander effect involves irradiating cells in culture and transferring some of the culture medium to unirradiated cells, which then respond as if they had been irradiated. The effect is absent if the irradiated medium contains no cells. The irradiated cells secreted some chemical into the medium that affected the unirradiated cells. In one such experiment, apoptosis was induced in the unirradiated culture by quite low doses to the irradiated cells. The dose response curve was nearly flat.

Another type of experiment used microbeams of α particles to irradiate specific cells in a culture, and then measured the response of neighboring cells which had not been irradiated. The survival of cells not irradiated decreased as their neighbors were hit with more α particles. It is thought that some chemical produced in the irradiated cells migrated into the unirradiated cells through gap junctions connecting the cytoplasm of neighboring cells. Similar experiments are done with radioactive nuclides that emit very-short range Auger electrons (see Chap. 17). The nuclides are attached to molecules that are selectively taken up by the cell nucleus or cytoplasm or that bond to the cell's DNA (Kassis 2004).

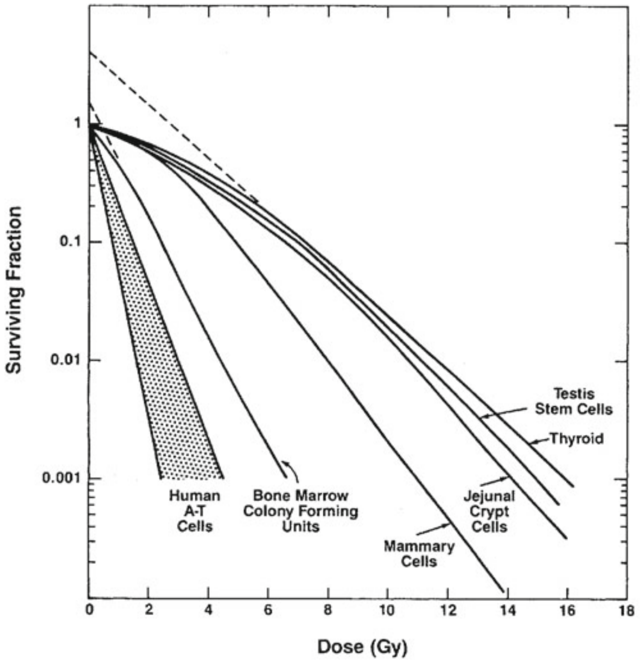

Fig. 16.34 Survival curves for assays of human cells. There is a wide range in initial sensitivity, but not too much difference in final slope. The shaded area labeled "human A-T cells" is for cells from a disease, ataxia-tangliectasia, where repair mechanisms are lacking. (Reproduced with permission from Hall 2002, p. 328)

16.9.5 Tissue Irradiation

There is considerable variation in the shape of the survival curves for human cells (Fig. 16.34). The shaded area labeled "human A-T cells" is for cells from patients with a genetic disease, *ataxia-tangliectasia*, where repair mechanisms are lacking and breakage of a single strand of DNA leads to cell death.

The radiation damage to the DNA is not apparent until the cell tries to divide. At that point, the chromosomes are either so badly damaged that the cell fails to divide or the damage survives in later generations as a mutation. Some tissues respond to radiation quite quickly; others show no effect for a long time. This is due almost entirely to the duration of the G_1 phase or the overall time between cells divisions. Tissues are divided roughly into two groups: *early-responding* and *late-responding*. Early-responding tissues include most cancers, skin, the small and large intestine, and the testes. Late-responding tissues include spinal cord, the kidney, lung, and urinary bladder.

The central problem of radiation oncology is how much dose to give a patient, over what length of time, in order to

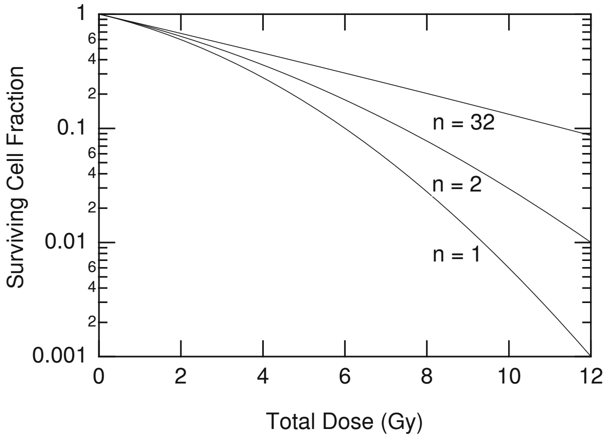

Fig. 16.35 The fraction of cells surviving a total radiation dose when the dose is divided into 1, 2, and 32 fractions, showing how the curve approaches $e^{-\alpha D}$ as the number of fractions becomes large

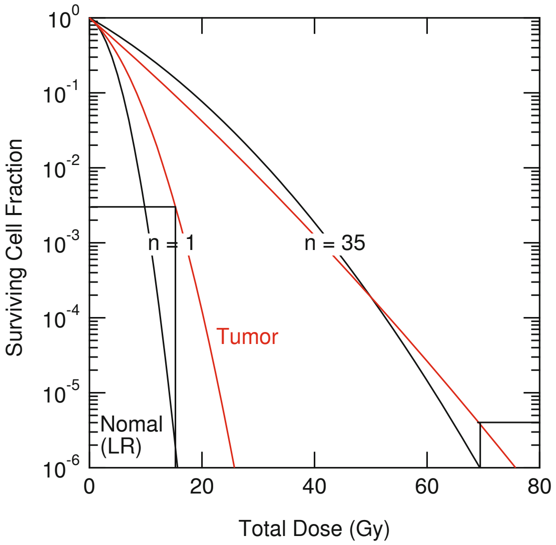

Fig. 16.36 Cell survival curves for late-responding normal tissue (*LR*) and for a hypothetical tumor (in red), showing the improvement obtained by dividing the dose into fractions. With a single fraction, the tumor survives much better than the normal tissue. With 35 fractions, this discrepancy has been reduced. The details are discussed in the text

have the greatest probability of killing the tumor while doing the least possible damage to surrounding normal tissue. While the dose is sometimes given all at once (over several minutes), it is usually given in *fractions* five days a week for four to six weeks. Some recent treatment plans, primarily for brachytherapy (see Sect. 17.11), use fractions given every few hours.

What total dose (or dose per fraction) should be given in how many fractions, with what time between fractions? We can gain some insight by using the linear-quadratic model. Let the dose per fraction be D_f, the number of fractions be n, and the total dose be $D = nD_f$. We plot survival vs. total dose for different numbers of fractions. We assume that the time between fractions allows for full repair of sublethal damage (single-strand breaks). The probability of a cell surviving after n fractions have been delivered is

$$P_s = P_{\text{survival}} = S = \left(e^{-\alpha D_f - \beta D_f^2}\right)^n = e^{-\alpha D - \beta D^2/n}. \tag{16.30}$$

As the number of fractions becomes very large for a given total dose, the survival curve approaches $e^{-\alpha D}$. This can be seen in Fig. 16.35, which plots survival vs. total dose delivered in different numbers of fractions. With many fractions the dose per fraction is very small, all the single-strand breaks are repaired, and almost no type-B cell deaths take place.

Early-responding tissue and tumors have been found to have an α/β ratio of about 10 Gy. The survival curve is primarily due to type-A damage. Late-responding tissues have an α/β ratio of 2–3 Gy. There is considerable variation in these numbers.

Some of the problems of radiation therapy and the benefits of fractionation can be seen if we consider a strictly hypothetical example (a toy model) in which $\alpha = 0.15$ Gy^{-1} for the tumor and 0.1 Gy^{-1} for the surrounding tissue. The tumor is early responding with $\alpha/\beta = 10$ Gy, and the surrounding tissue is late responding with $\alpha/\beta = 2$ Gy. Figure 16.36 shows the cell-survival curves for 1 and 35 fractions. The tumor survival in each case is shown in red.

To see the benefit of fractionation, suppose that the patient can tolerate a dose at which only 10^{-6} of the cells of the surrounding tissue survive, represented by the horizontal line on the graph. (This is not realistic!) For a single fraction, this corresponds to a total dose of about 15 Gy, which, applied to the red line, shows that the surviving fraction of tumor cells is about 3×10^{-3}. For 35 fractions the normal tissue can tolerate about 70 Gy, yielding 4×10^{-6} as the fraction of tumor cells surviving.

Suppose next that it is possible to confine the radiation beam so that the dose to normal tissue is only about 0.6 times that to the tumor. This means that the tissue dose in Eq. 16.30 is multiplied by 0.6. The result is shown in Fig. 16.37 for 35 fractions. The tumor dose can now be as high as 115 Gy for the same effect on surrounding tissues, leading to a tumor survival of only 10^{-10}. We will see how beam shaping is accomplished in the next section.

These calculations are solely to illustrate the basic principles, and the doses are not realistic. Clinically useful calculations must take several additional factors into account: the actual values of α for the tissue and tumor under consideration, the effect of cell growth after irradiation, the effect of the first dose on synchronizing the cycles of the remaining cells, and the oxygen level in the tumor cells. (The greater

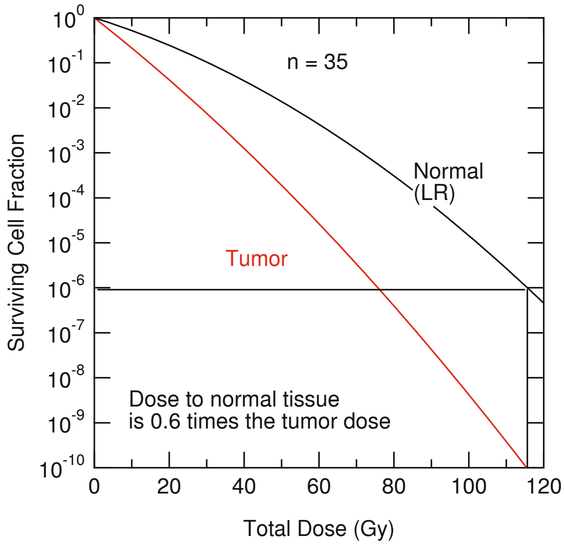

Fig. 16.37 Survival curves for the same cells as in the previous figure, with the dose to the surrounding tissue reduced to 0.6 times that to the tumor. Now the probability of tumor survival at high doses is about 0.0001 times that for the surrounding normal tissue. This shows the importance of confining the radiation to the tumor as much as possible

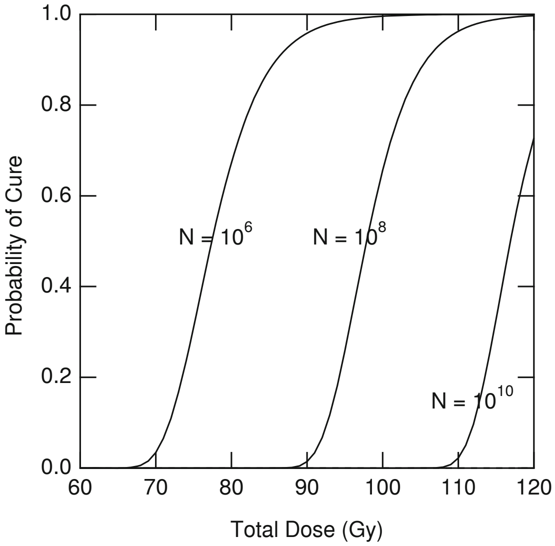

Fig. 16.38 The probability of eradicating the tumor (no surviving tumor cells) as a function of dose for tumors containing different numbers of cells

the oxygen concentration the more sensitive the cells are, particularly for low-LET radiation. Rapidly growing tumors often outstrip their blood supply, receive less oxygen, and are less radio-sensitive.) Fractionation is reviewed in Orton (1997) and in Hall and Giaccia (2012). It is also necessary to take into account the fact that neither the tumor nor the surrounding normal tissue receives a uniform dose of radiation.

16.9.6 A Model for Tumor Eradication

The target theory model can be applied to a collection of cells to give us insight into the central problem of radiation therapy: *tumor eradication*. Suppose that a tumor consists of N cells with identical properties. The cells are uniformly irradiated with dose D. If a collection of identical tumors were irradiated, the number of cells surviving in each tumor would fluctuate. The probability that a single cell survives is $p_s(D)$, which might be given by Eq. 16.30. If this number is small and N is large, the number surviving follows a Poisson distribution. The average number surviving is $m = Np_s(D)$. The probability of a cure is the probability that no tumor cells survive:

$$P_{\text{cure}} = e^{-m} = e^{-Np_s(D)}. \qquad (16.31)$$

This can be evaluated using your cell-survival model of choice.

Figure 16.38 shows a tumor eradication curve based on the 35-fraction curve in Fig. 16.36. The larger the tumor, the greater the dose required for cure. Figure 16.39 shows a plot of the probability of tumor cure and the probability of unacceptable damage to the surrounding tissue. For this example, at least 60 Gy are required in order to have a good probability of cure; once the dose is higher than 63 Gy, the damage to normal tissue is unacceptable.

16.10 Radiation Therapy

The treatment of cancer must deal with two issues: eradication of the primary tumor (*local control*), and eradication of *metastases*, which may be in nearby tissue or may be at distant sites in the body. In many cases radiation therapy, either alone or combined with surgery, is the best technique for local control. Two oncologists have provided a review of the benefits and problems of radiation therapy, addressed specifically to the medical physics community (Schulz and Kagan 2002). They point out that many cancer deaths are due to metastatic disease, so improved local control does not necessarily provide a corresponding improvement in survival. Ratliff (2009) provides a survey of literature about radiation therapy.

Which method of treatment is best can change dramatically as new treatments are developed. For example, a combination of radiation therapy and chemotherapy was once used to treat Hodgkin's disease; chemotherapy has been improved to the point where radiation is no longer necessary (DeVita 2003).

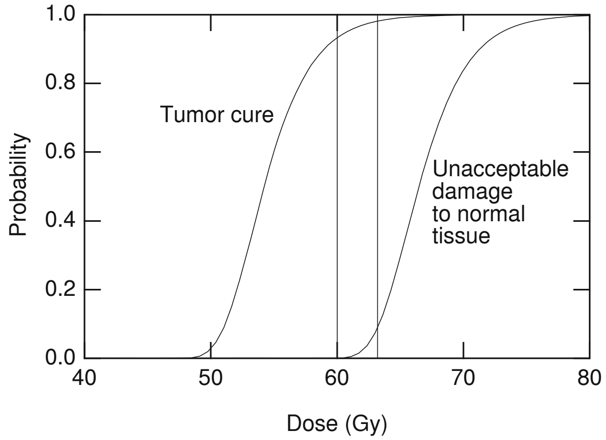

Fig. 16.39 The probability of curing the tumor and the probability of unacceptable damage to normal tissue vs. dose

Fig. 16.40 X-ray therapy was used to treat a carcinoma of the nose. *A* shows the original lesion; *B* is the result one year later. The patient remained asymptomatic 5 years after treatment. (Reprinted from William and James 1989, with permission from Elsevier)

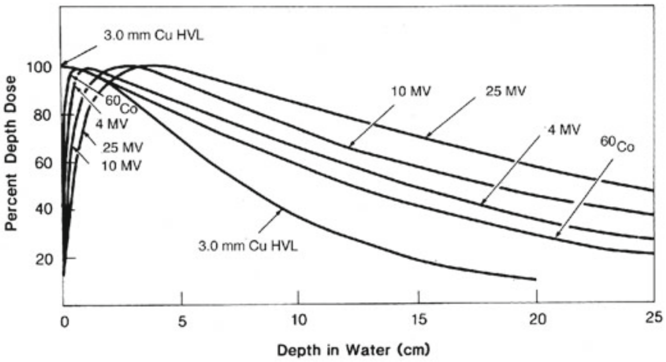

Fig. 16.41 The dose vs. depth for x-ray beams of different quality (energy) on the central axis of the beam. The source–surface distance (SSD) is 100 cm and the field size is 10×10 cm. The curve "3.0 mm Cu HVL" is for a photon beam that is reduced to half intensity by a copper filter 3.0 mm thick. The radioactive element ^{60}Co emits two gamma ray photons (1.17 and 1.33 MeV.) The labels 4, 10 and 25 MV refer to the energy of the electron beam striking the x-ray tube anode. (From Khan 2003, p.163. ©2003 Lippincott Williams & Wilkins)

16.10.1 Classical Radiation Therapy

Doses for diagnostic radiology vary from about 10^{-4} to 10^{-2} Gy. Doses of 20–80 Gy are required to treat cancer. A great deal of physics is involved in planning the treatment for each patient [See Khan (2010) or Goitein (2008)]. There is a choice of radiation beams: photons of various energies, electrons, neutrons, protons, or α particles. Photons and electrons are routinely available; the other sources require special facilities. The number of proton facilities is growing rapidly. Only a few of the beam issues will be raised here. Some of the dose measurement issues are discussed in the next section.

An example of the effectiveness of radiation therapy is shown in Fig. 16.40 The patient developed a carcinoma of the nose and refused surgery. Radiation with a total dose of 50 Gy was used, and the results one year later are shown. It is ironic that the carcinoma probably developed because the patient was treated with x-rays for acne many years earlier.

We have already seen the importance of reducing dose to tissue surrounding the tumor. Optimizing the dose determines the kind of radiation to be used and its energy, as well as the details of beam filtration and collimation and how it is aimed at the patients body. For now, we discuss a photon beam. Attenuation and the $1/r^2$ decrease of photon fluence help spare tissue downstream in the beam. Since μ_{atten} decreases with increasing photon energy up to a few MeV, higher-energy photons penetrate more deeply and must be used for treating deeper lesions. There is also dose buildup with depth over distances comparable to the range of the Compton-scattered electrons. Both of these effects are shown in Fig. 16.41.

The beam is *collimated* to spare normal tissue. Originally, the collimator consisted of four lead jaws that provided a rectangular opening with adjustable length and width. A wedge was sometimes placed in the beam to vary the intensity across the collimated radiation field.

Figure 16.42 shows *isodose contours* for various beams. In addition to the differences with depth seen in Fig. 16.41, there are significant differences in the sharpness of the dose distribution across the beam. The extent of the lesion to be radiated must be carefully determined with radiographs or CT scans.

If the tumor is not near the surface, the ratio of tumor dose to normal tissue dose can be increased by irradiating the patient from several directions. Figure 16.43 shows how the relative dose to a deep tumor can be increased by irradiating with two *fields* on opposite sides of the patient. In Fig. 16.44

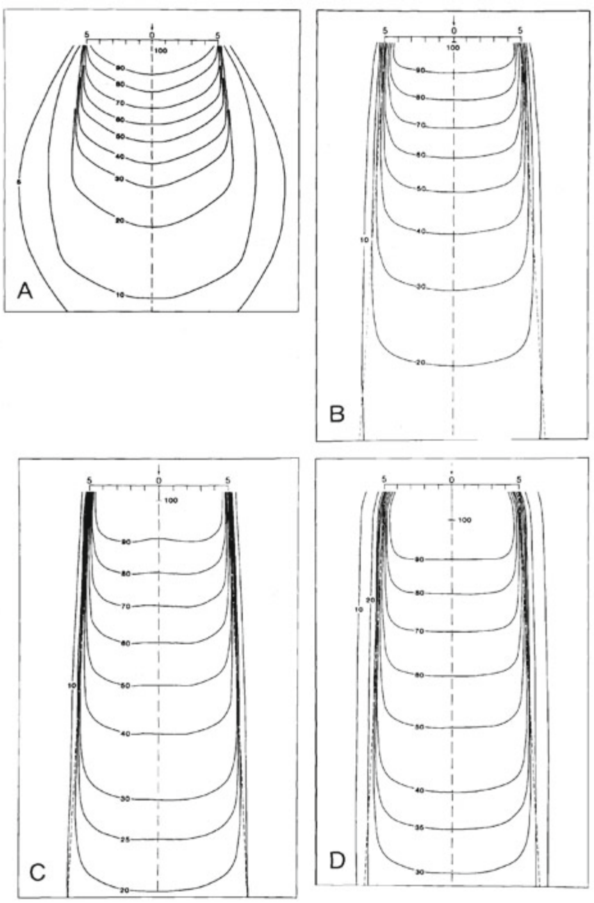

Fig. 16.42 Isodose distributions for radiation under different conditions, all collimated to 10×10 cm. **a** Radiation from an x-ray tube with 200 kVp, 0.5 m from the surface. **b** Photons from the radioactive isotope ^{60}Co, 0.8 m from the surface. **c** 4-MV photons, 1 m from the surface. **d** 10-MV photons, 1 m from the surface. (From Khan (2003, p. 204). ©2003 Lippincott Williams & Wilkins)

three and four fields are used. The angles of the fields can be changed by rotating the patient couch as well as the gantry holding the photon source and collimator.

Rectangular fields do not match the shape of the tumor. To overcome this problem a *multileaf collimator* replaces the four original jaws on the therapy machine. A typical multileaf collimator has up to 100 pairs of tungsten alloy leaves, each a few mm wide, which can be independently adjusted to provide a pattern like that in Fig. 16.45. This might be used for up to nine fields from different directions.

16.10.2 Modern X-Ray Therapy

The goal of radiation therapy is to provide as large a dose as possible to the tumor while sparing adjacent normal tissue.

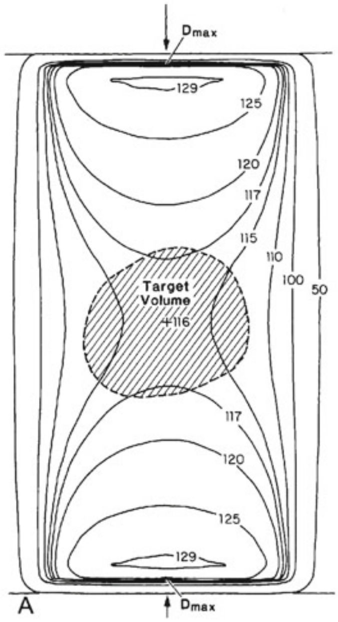

Fig. 16.43 Isodose distribution when the patient is irradiated equally from opposite sides. (From Khan (2003, p. 210). ©2003 Lippincott Williams & Wilkins)

The normal tissue may be quite close to the tumor. *Three-dimensional conformal radiation therapy* uses 3-dimensional information about the target volume. This is difficult, because even with 3-dimentional display of CT, MRI or ultrasound images, it may be impossible to see the edges of the tumor. Nevertheless, the *beam's-eye view* that can be computed from 3-d image data can be very useful in planning the treatment. For a discussion of conformal radiation therapy, see Khan (2010), Chap. 19.

In classical radiotherapy, the beam was either of uniform fluence across the field, or it was shaped by an attenuating wedge placed in the field. *Intensity-modulated radiation therapy* (IMRT) is achieved by stepping the collimator leaves during exposure so that the fluence varies from square to square in Fig. 16.45 (Goitein 2008; Khan 2010, Ch. 20)

It was originally hoped that CT reconstruction techniques could be used to determine the collimator settings at different angles. This does not work because it is impossible to make the filtered radiation field negative, as the CT reconstruction would demand. IMRT with conventional treatment planning improves the dose pattern (Goitein (2008); Yu et al. (2008)), providing better sparing of adjacent normal tissue and allowing a boost in dose to the tumor.

One problem in radiation therapy is movement of organs when the patient breathes. Four-dimensional CT records data at a fixed point in the respiratory cycle. The radiotherapy beam is turned on only at the same point in the cycle (Khan 2010, Ch. 25).

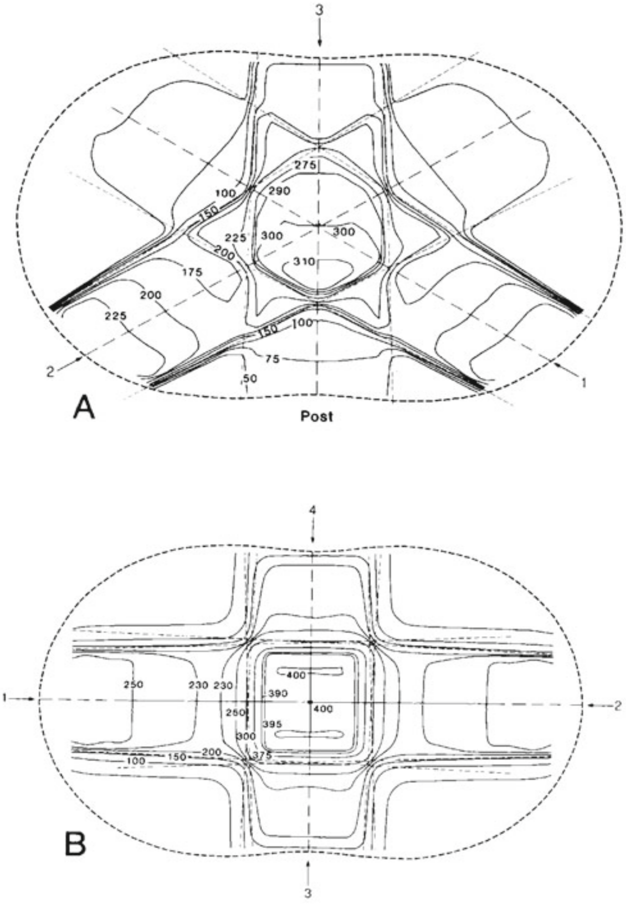

Fig. 16.44 Isodose distribution for (**a**) three and (**b**) four radiation fields, each designed to give a relative dose of 100 at the center of the tumor. (From Khan 2003, p. 215. © 2003 Lippincott Williams & Wilkins)

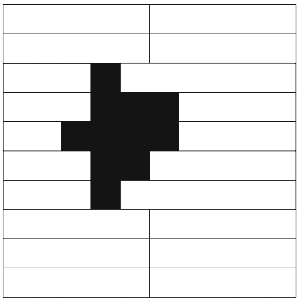

Fig. 16.45 A multileaf collimator (MLC). The tungsten leaves are shown in white; the opening is black

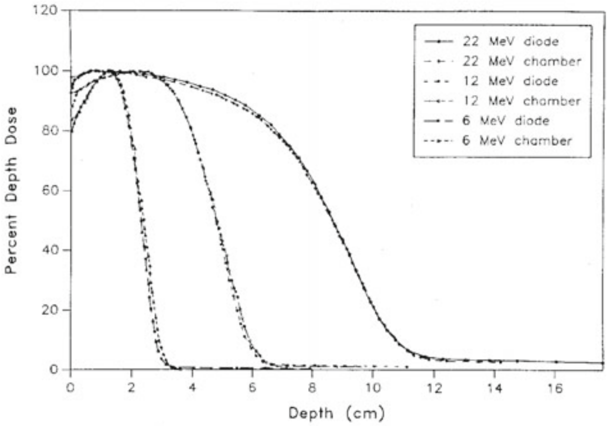

Fig. 16.46 Depth–dose curves for electrons of different energies, measured with a solid-state detector (diode) and an ionization chamber. Both the range and the straggling increase with increasing energy. (From F. M. Khan 1986). AAPM Monograph 15.

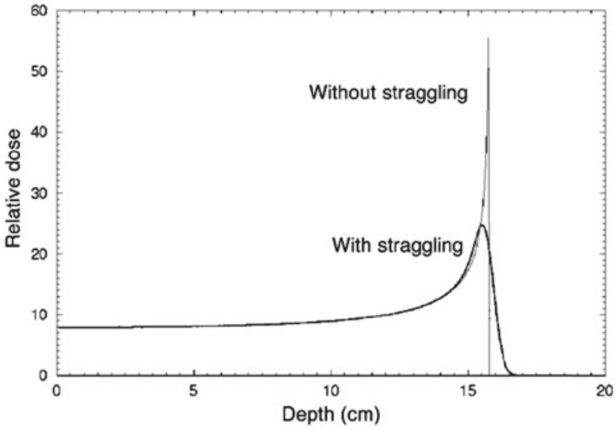

Fig. 16.47 Energy loss vs. depth for a 150 MeV proton beam in water, with and without straggling. The Bragg peak enhances the energy deposition at the end of the proton range. (Copyright © 2005 W. D. Newhauser, M. D. Anderson Cancer Center. Used by permission)

16.10.3 Charged Particles and Neutrons

Electrons, typically between 6 and 20 MeV, are also used for therapy (Hogstrom and Almond (2006)). Because of the range–energy relationship, the field falls nearly to zero in a few centimeters. Electrons are used primarily for skin and lip cancer, head and neck cancer, and irradiation of lymph nodes near the surface. Figure 16.46 shows the dose vs. depth as a percent of the maximum dose for electron beams of several different energies.

Protons are also used to treat tumors (Khan 2010, Ch. 26; Goitein 2008). Their advantage is the increase of stopping power at low energies. It is possible to make them come to rest in the tissue to be destroyed, with an enhanced dose relative to intervening tissue and almost no dose distally ("downstream") as shown by the *Bragg peak* in Fig. 16.47. Placing an absorber in the proton beam before it strikes the patient moves the Bragg peak closer to the surface. Various

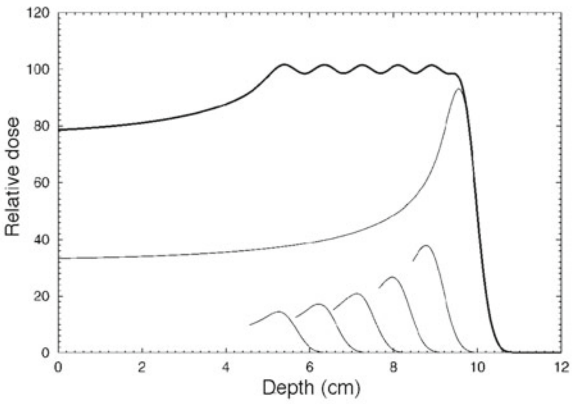

Fig. 16.48 Irradiating the patient through a number of absorbers of different thickness spreads out the region of maximum dose. (Copyright © 2005 by W. D. Newhauser, M. D. Anderson Cancer Center. Used by permission)

techniques, such as rotating a variable-thickness absorber in the beam, are used to shape the field by spreading out the Bragg peak (Fig. 16.48). The edges of proton fields are sharper than for x-rays and electrons (Delaney and Kooy 2008). This can provide better tissue sparing, but it also means that alignments must be more precise. Another technique is to extract the protons from the accelerator at the desired energy and use magnets to sweep the resulting beam across the desired region of the patient (Goitein 2008).

Sparing tissue reduces side effects immediately after treatment. It also reduces the incidence of radiation-induced second cancers many years later. These are particularly important in pediatric patients as the initial treatment proves more successful and the patients survive longer. Miralbell et al. (2002) estimated the incidence rate for secondary cancers in certain pediatric cancers and found a reduced incidence for proton therapy compared to both conventional x-ray and IMRT.

Proton therapy is used in a number of diseases. Delaney and Kooy (2008) provide an extensive review. Some institutions are experimenting with intensity-modulated proton therapy (IMPT) (Xu et al. 2008).

Fast neutrons are used for therapy (Duncan 1994). The dose is due to charged particles: protons, α particles (^{4}He nuclei), or recoil nuclei of oxygen and carbon that result from interactions of the neutrons with the target tissue. All of these have high LET, and the oxygen effect is less than for low-LET radiation. Fast neutron therapy shows promise in some salivary gland cancers (Douglas et al. 2003).

Boron neutron capture therapy (BNCT) is based on a nuclear reaction which occurs when the stable isotope ^{10}B is irradiated with neutrons, leading to the nuclear reaction (in the notation of Chap. 17)

$$^{10}_{5}\mathrm{B} + ^{1}_{0}n \rightarrow ^{4}_{2}\alpha + ^{7}_{3}\mathrm{Li} \qquad \text{or} \qquad ^{10}_{5}\mathrm{B}(n,\alpha)^{7}_{3}\mathrm{Li}.$$

Both the alpha particle and lithium are heavily ionizing and travel only about one cell diameter. BNCT has been tried since the 1950s; success requires boron-containing drugs that accumulate in the tumor. The field has been reviewed by Barth (2003).

Brachytherapy (brachy means short) involves the implantation of radioactive isotopes in a tumor and will be discussed in Chap. 17.

16.11 Dose Measurement

It is important to measure radiation doses accurately for radiation therapy in order to compare the effectiveness of different treatment protocols and to ensure that the desired protocol is indeed being followed. Accuracies of 2 % are expected. An extensive literature about relating the dose in the measuring instrument to the dose in surrounding tissue exists.[20] Here we describe one of the techniques that is used.

A basic problem in dosimetry is that the measuring instrument has different properties than the medium in which it is immersed. Imagine, for example, that a gas-filled ionization chamber is placed in water. If the radiation field were very large and uniform, one could in principle use an ionization chamber whose dimensions are large compared to the range of secondary electrons, and the interaction of the radiation field with the chamber gas would be the dominant effect. This is not practical. At the other extreme, we imagine an ionization chamber that is so small that it does not alter the radiation field of the water. That is, its dimensions must be small compared to the range of the charged particles created in the water and passing through it.

We saw in Sect. 15.16 that the absorbed dose in a parallel beam of charged particles with particle fluence Φ is (Eq. 15.75)

$$D = \frac{S_e}{\rho}\Phi.$$

Usually the beam consists of particles with different kinetic energies T. Let Φ_T be the energy spectrum:

$$\Phi = \int_0^{T_{\max}} \Phi_T \, dT.$$

Then the dose is the integral of the number of particles with energy T times the mass stopping power for particles of that

---

[20] See Attix (1986), Chap. 10ff or Khan (2010), Chap. 8.

energy:

$$D = \int_0^{T_{\max}} \Phi_T \frac{S_e}{\rho}\, dT. \tag{16.32}$$

We can define an average mass collision stopping power:

$$\frac{\overline{S}_e}{\rho} = \frac{1}{\Phi} \int_0^{T_{\max}} \Phi_T \frac{S_e}{\rho}\, dT \tag{16.33}$$

so that

$$D = \Phi \frac{\overline{S}_e}{\rho}. \tag{16.34}$$

Let us apply this to the situation where a small detector ("gas") is introduced in a medium ("water") in which we want to know the dose. The charged particle fluence is not altered by the detector because it is small compared to the range of the charged particles. Applying Eq. 16.34 in both media, we obtain

$$\frac{D_w}{D_g} = \frac{(\overline{S}_e/\rho)_w}{(\overline{S}_e/\rho)_g} \equiv (\overline{S}_e/\rho)_g^w. \tag{16.35}$$

This is the *Bragg–Gray relationship* for the absorbed dose in the cavity. It is standard in the literature to denote the dimensionless ratio of the stopping powers in the two media by $(\overline{S}_e/\rho)_g^w$ [or, in some books, $(\overline{S}_c/\rho)_g^w$].

This equation is often used with ionization chambers. The charge created in an ionization chamber of mass m is the charge per ion pair e times the number of ion pairs formed in mass m. The number of ion pairs is the energy deposited, mD_g, divided by the average energy required to produce an ion pair, W:

$$q = e\frac{mD_g}{W}. \tag{16.36}$$

Combining this with Eq. 16.35 gives the dose in the medium in terms of the charge created:

$$D_w = \frac{q}{m}\left(\frac{W}{e}\right)_g (\overline{S}_e/\rho)_g^w. \tag{16.37}$$

The charge q created is usually greater than the charge collected in the ion chamber because of recombination of ions and electrons before collection. The collection efficiency and the chamber mass are deduced from calibration of the chamber. Once the chamber has been calibrated, the factor $(\overline{S}_e/\rho)_g^w$ accounts for placing the chamber in different media.

16.12 The Risk of Radiation

Exposure to radiation may or may not cause a noticeable effect. Effects can include a change, which may not be harmful; damage to cells, which may not necessarily be deleterious to the individual; or harm, which is clinically observable in the subject or possibly a descendant (though current data suggest that genetic changes are rare). It may take years before the harm is observed. The International Commission on Radiological Protection in ICRP (1991) defines the *detriment* to an individual who receives a dose of radiation. It is a rather complex combination of the probability of harm, the severity of the harm, and the time of onset after exposure. It will be discussed more below.

In this section we focus on the increased probability of induction of cancer from an exposure to radiation. We have considerably more information about human exposure to ionizing radiation than we have for any other known or suspected carcinogen (Boice 1996). Several studies at moderate doses show that radiation is a relatively weak carcinogen, though this is not the public view.

We have already seen that the biological effect of radiation depends on the absorbed dose, the LET, the nature of the tissue that is irradiated, and the dose rate. It also depends on the age of the subject. This makes it very difficult to estimate the detriment. Ideally, we would multiply the dose to each organ or target in the body by the probability of a detriment to that target from that kind of radiation now and in the future, and sum over all the organs in the body. This is impossible: we do not know enough. We must simplify the problem while taking some of these differences into account.

16.12.1 Equivalent and Effective Dose

16.12.1.1 Equivalent Dose

Our first simplification assumes that the LET dependence is the same for all target organs. ICRP defines the *radiation weighting factor* W_R for each radiation type R striking the body. It depends on the radiation type and energy and is independent of organ or tissue type. The radiation weighting factor for x-rays is 1. W_R is determined "with guidance" from an earlier quantity, the *relative biological effectiveness* of the radiation (RBE). The weighting factor for each radiation W_R is multiplied by the average dose to the target organ or tissue $D_{R,T}$ and summed to give the *equivalent dose*[21] to

---

[21] The nomenclature here is quite confusing. ICRP used to define the *dose equivalent*, also denoted by H, as QD, where Q was called the *quality factor* of the radiation. The radiation weighting factor is very similar, and essentially numerically equivalent, to the earlier quality factor, Q. Values of Q recommended by Nuclear Regulatory Commission (NRC) are 1 for photons and electrons, 10 for neutrons of unknown energy and high-energy protons, and 20 for α particles, multiply charged ions, fission fragments, and heavy particles of unknown charge. The ICRP has its own recommendations, that differ slightly for protons and neutrons. See McCollough and Schueler (2000).

Table 16.4 Contribution of some organs to the whole-body radiation detriment. (From ICRP 1991, Table B-20)

Organ (T)	Cancer probability, per Sv	Severe genetic probability, per Sv	Corrected for life lost and nonfatal cancers, per Sv	Tissue weighting factor (W_T)
Bladder	30×10^{-4}		29.4×10^{-4}	0.04
Breast	20×10^{-4}		36.4×10^{-4}	0.05
Stomach	110×10^{-4}		100×10^{-4}	0.14
Gonads		100×10^{-4}	133×10^{-4}	0.18
Total	500×10^{-4}		752×10^{-4}	1.00

the target organ, H_T:

$$H_T = \sum_R W_R D_{R,T}. \tag{16.38}$$

The unit of H_T is the *sievert* (Sv).[22]

16.12.1.2 Detriment and Effective Dose

The detriment is a measure of the harm from an exposure to radiation. It might be a genetic effect (relatively rare) or the development of cancer some years later. If cancer, it might be fatal, shortening life span, or it might cause discomfort and inconvenience but not death. We want to estimate the detriment when a certain equivalent dose has been delivered to some target organs. We assume that the probability of developing cancer in a target organ depends on the dose to that organ and not on the dose to any other part of the body. We also assume that the probabilities are small, so that if several organs have received a radiation dose, the probability of developing cancer is the sum of the probabilities for each organ.

Most of our information about the detriment comes from extensive studies of atomic-bomb survivors, for whom the entire body received a fairly uniform equivalent dose. These survivors have now been followed for almost 70 years. Other studies include patients who have been followed for decades after receiving radiation therapy. ICRP (1991) estimates the radiation detriment using these data and taking into account the probability of a fatal cancer attributable to the radiation, the weighted probability of an attributable nonfatal cancer, the weighted probability of severe hereditary effects, and the relative decrease in lifespan. Table 16.4 shows four of the 14 entries in Table B-20 of ICRP (1991). The details of the various corrections are not shown; the point is to show how each organ contributes to the total detriment.

If a uniform dose is given to the entire body, some organs are more sensitive to the radiation than others. The *effective dose*[23] E is a sum over all irradiated organs:

Table 16.5 Major contributions to the effective dose from a typical CT head scan

Organ	W_T	H_T (mSv)	$W_T H_T$ (mSv)
Brain	0.025	36	0.90
Bone marrow (red)	0.12	3	0.36
Thyroid	0.05	5.5	0.28
Bone surface	0.01	14	0.14
All other organs			0.10
Effective dose			1.8

$$E = \sum_T W_T H_T = \sum_{R,T} W_T W_R D_{R,T}. \tag{16.39}$$

The *tissue weighting factor* W_T is the radiation detriment for organ T from a whole body irradiation as a fraction of the total radiation detriment. By definition, the sum of W_T over all organs equals unity. The last column of Table 16.4 shows the W_T assigned to each target organ in ICRP (1991). See also the review by McCollough and Schueler (2000). Slightly different values of W_T are found in ICRP (2007), Table B.2.

As an example, consider a typical CT head scan, which provides a significant equivalent dose to the brain, bone marrow, thyroid, and bone surface, as shown in Table 16.5.[24] The effective dose is 1.8 mSv. The probability of developing a radiation-induced cancer is $500 \times 10^{-4} \times 1.8 \times 10^{-3} = 9 \times 10^{-5}$. If the whole body were to receive an equivalent dose of 36 mSv, the probability of a radiation-induced cancer would be $500 \times 10^{-4} \times 36 \times 10^{-3} = 1.8 \times 10^{-3}$.

16.12.2 Comparison With Natural Background

One way to express risk is to compare medical doses to the natural background. We are continuously exposed to radiation from natural sources. These include cosmic radiation, which varies with altitude and latitude; rock, sand, brick, and

---

[22] Both the sievert and the gray are J kg^{-1}. Different names are used to emphasize the fact that they are quite different quantities. One is physical, and the other includes biological effects. An older unit for H is the rem. 100 rem = 1 Sv.

[23] An older, related quantity is the effective dose equivalent, $H_E = W_T Q D$.

[24] Values of H_T were provided by C. McCollough.

Table 16.6 Typical radiation doses from natural sources

Radiation source	Detail	Effective dose rate to target organ (mSv year^{-1})	US population average effective dose rate in 2006 (mSv year^{-1})[a]
Cosmic radiation	New York city	0.30	0.33
	Denver (1.6 km)	0.50	
	La Paz, Bolivia (3.65 km)	1.8	
	Flying at 40,000 ft	7×10^{-3} mSv hr^{-1}	
Terrestrial (radioactive minerals)			0.21
	Over fresh water	0	
	Over sea water	0.2	
	Sandy soil	0.1–0.25	
	Granite	1.3–1.6	
In the body			0.29
Inhalation of radon			2.28
Total			3.11

[a] NCRP Report 160 (2009) Table 1.1

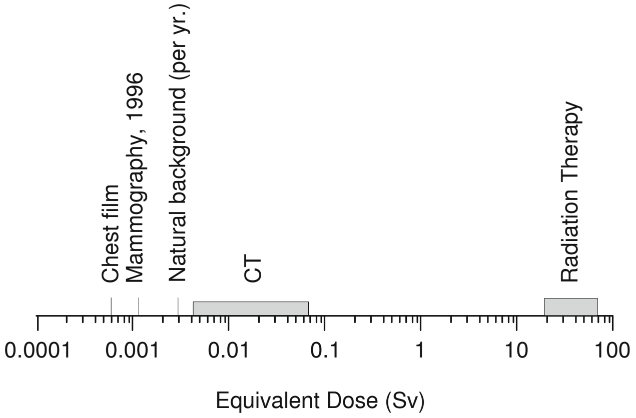

Fig. 16.49 Various doses on a logarithmic scale. Natural background is per year; other doses are per exposure

Table 16.7 Typical radiation equivalent doses for the population of the USA. (From AAPM Report 96 2008, Table 2)

Procedure	Equivalent dose (mSv)
Chest X-ray (Anterior Posterior)	0.1–0.2
Lumbar spine	0.5–1.5
Mammogram	0.3–0.6
Barium enema	3–6
Nuclear medicine cardiac	13–40
Head CT	1–2
Chest CT	5–7
Abdomen CT	5–7
Coronary CT angiography	5–15

concrete containing varying amounts of radioactive minerals; the naturally occurring radionuclides in our bodies such as ^{14}C and ^{40}K; and radioactive progeny from radon gas from the earth.[25] In a typical adult, there are about 4×10^7 radioactive disintegrations per hour from all internal sources. Table 16.6 and Fig. 16.49 summarize the various sources of radiation exposure. The radon entry in Table 16.6 is based on a W_R of 20 for α particles from radon progeny, the value used by NCRP.[26] There is considerable uncertainty in this determination: W_R could be as low as 3, in which case radon would contribute much less to the natural background.

Diagnostic procedures give doses that are in general comparable to the average annual background dose, as can be seen in Table 16.7. Mettler et al. (2008) give a more extensive set of doses. The higher CT doses correspond to pediatric CT; see Fig. 16.52. One can explain to a patient that a chest x-ray is equivalent to about 1 week of natural background, and a mammogram is equivalent to a month or two. A conventional fluoroscopic study of the lower digestive system is equivalent to about a year of natural background. ICRU Report No. 74 discusses patient dosimetry for medical imaging. There is a wide range of doses for a given procedure (Mettler 2008). Patients are having more and more radiologic examinations. Several steps are now taken to reduce the dose due to CT procedures. The cross-section of the body is elliptical; the x-ray tube current can be reduced when the path through the body is shorter. The overall tube current can be reduced as long as the photon-noise-limited resolution is good enough to identify the anatomy of interest.

---

[25] Radon is chemically inert gas that escapes from the earth. Since it is chemically inert, we breathe it in and out. When it decays in the air (the decay scheme is described in Sect. 17.12), the decay products attach themselves to dust particles in the air. When we breathe these dust particles, some become attached to the lining of the lungs, irradiating adjacent cells as they undergo further decay.

[26] The dose to the lungs from radon progeny is about 1 mGy yr^{-1}. This is multiplied by $W_r = 20$ and $W_T = 0.12$ (lungs) to arrive at an effective dose of 2.4 mSv yr^{-1}.

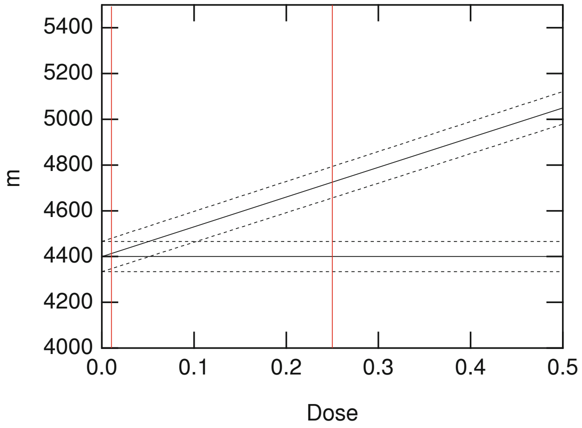

Fig. 16.50 Plot of the average number of cases from a population N for a linear no-threshold and a constant model. The *dashed lines* represent the mean ±1 standard deviation

16.12.3 Calculating Risk

Assessing the risk of radiation is complicated, since a radiation-induced cancer, for example, may not appear for many years. It is therefore necessary to specify how many years one watches a population after exposure, age at exposure, and current age. One also has to specify whether the risk is of acquiring the disease or of dying from it. Whatever criteria we use, we can define a risk $r(H)$ that depends on the equivalent dose. We then define the *excess absolute risk* as

$$EAR = r(H) - r(0) \tag{16.40}$$

and the *excess relative risk* as

$$ERR = \frac{r(H) - r(0)}{r(0)} = \frac{r(H)}{r(0)} - 1 = \frac{EAR}{r(0)}. \tag{16.41}$$

The units of r and excess absolute risk can vary. The risk might be per person per year, or it might be for a certain number of years or for a lifetime exposure. The excess relative risk has the advantage of being dimensionless. It is frequently reported, even though it can be difficult to understand intuitively. (Plots of EAR vs. dose for breast cancer in Japanese women and women in the USA have nearly the same slope. However, $r(0)$ is smaller for Japanese women, leading to a higher ERR).

Consider a rare disease, and suppose that the probability of acquiring the disease over a lifetime is 2×10^{-3}, while in a population that has received a particular dose of something (which might be radiation, or a chemical, or a particular behavior) the probability is 5×10^{-3}. Then the excess absolute risk is 3×10^{-3}, while the excess relative risk is 150 %. A person hearing that the relative risk has increased by 1.5 times might be unduly alarmed, not realizing that there are only three additional cases in 1000 people.

Statistical fluctuations can make it quite difficult to measure excess risk. Suppose that we want to determine whether r increases linearly with dose. Measurements at lower doses to determine if the response is linear are difficult to make, requiring large numbers of subjects, as the following simplified example shows. Suppose that we have two measurements of the probability of acquiring cancer: one at zero dose, which gives $r(0)$, the "spontaneous" probability due to nonradiation causes, and one at a fairly large dose (say 0.25 Sv, represented by the vertical red line on the right in Fig. 16.50). At some lower dose we want to make a measurement to distinguish between a linear increase of probability with dose and a probability that remains at the "spontaneous" value because we are below some threshold dose for carcinogenicity. The probability $p = r(H)$ of acquiring cancer is small, and the total population N is large. This means that if the experiment could be repeated several times on identical populations, the number of persons acquiring cancer, n, would be Poisson distributed with mean number $m = Np = Nr(H)$ and standard deviation $\sigma = \sqrt{m}$. Figure 16.50 plots m vs. dose for some value of N, with dotted lines to indicate $m \pm \sigma$. A measurement at the lower dose indicated by the vertical red line on the left will not distinguish between the two curves. The only way to reduce the width between the dotted lines at $m \pm \sigma$ would be to use a larger population N.

To give a quantitative but overly simplified example, suppose that $r(H) = e + \alpha H$, with $e = 0.044$ and $\alpha = 0.013\ \text{Sv}^{-1}$. At a dose of 0.25 Sv, $r = 0.047$. For 10^5 persons, the constant curve (expected in the absence of radiation or below threshold) gives $m = 4400 \pm 66$, while the linear curve gives $m = 4730 \pm 69$. The two curves are distinguishable. At a dose of 0.01 Sv, m for the constant curve is still 4400 ± 66, while for the linear case it is 4410 ± 66. It is impossible to distinguish between the linear and constant curves.

16.12.3.1 The Linear No-Threshold Model and Collective Dose

In dealing with radiation to the population at large, or to populations of radiation workers, the policy of the various regulatory agencies has been to adopt the *linear no-threshold* (LNT) model to extrapolate from what is known about the excess risk of cancer at moderately high doses and high dose rates, to low doses, including those below natural background.

If the excess probability of acquiring a particular disease is αH in a population N, the average number of extra persons with the disease is

$$m = \alpha N H. \tag{16.42}$$

The product NH, expressed in person Sv, is called the *collective dose*. It is widely used in radiation protection, but it is meaningful only if the LNT assumption is correct. Small doses to very large populations can give fairly large values of

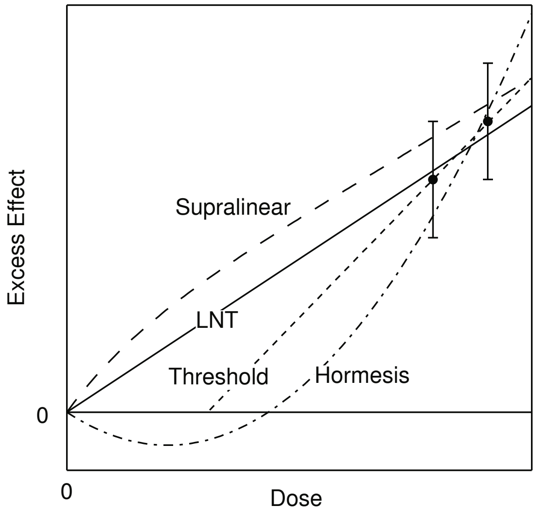

Fig. 16.51 Possible responses to various doses. The two lowest-dose measurements are shown. With zero dose there is no excess effect. The curves are discussed in the text

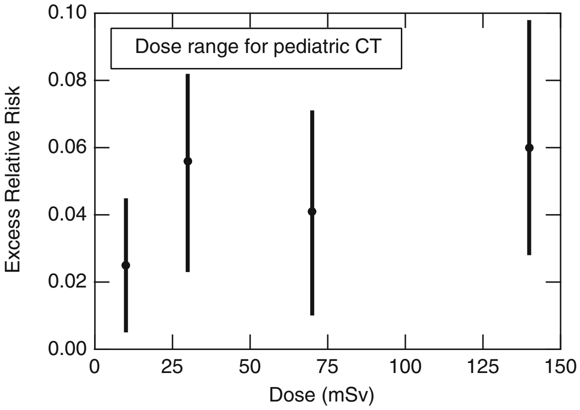

Fig. 16.52 Excess relative risk for atomic bomb survivors who were exposed to a dose of 150 mSv or less and followed for 55 years show a small, but statistically significant increase in cancer incidence. The range of doses from pediatric CT is also shown. (Redrawn from Hall (2002, pp. 225–227). With kind permission of Springer Science and Business Media)

m, assuming that the value of α determined at large doses is valid at small doses.

It has been suggested that there may in some cases be a threshold for radiation-induced damage. If there is a threshold, then the LNT model gives an overestimate. The latest reports of expert panels continue to recommend the LNT model (NCRP Report 136 2001; Upton 2003; BEIR Report VII 2005), but their recommendation is still questioned (Higson 2004; Tubiana et al. 2009). The debate about the LNT model continues (Doss et al. 2014).

To help put the risk in perspective, consider the following example from BEIR (2005), p. 15. Among 100 people, about 42 will be diagnosed with cancer during their lifetime in the absence of any excess radiation. If they had all received a dose of 0.1 Gy (100 mSv for low-LET radiation), there could be one additional cancer in the group.

Even if the LNT model is correct, it can lead to regulatory decisions that are not reasonable. For example, Brooks (2003) cites a study in which the process of cleaning up several Department of Energy sites resulted in more fatal worker accidents than the number of lives that were calculated to have been saved, based on the LNT model.

The Health Physics Society (2010) issued a position statement that radiogenic health effects have not been consistently demonstrated below 100 mSv. They recommend that estimates of risk should be limited to individuals who receive a dose of 50 mSv in one year or 100 mSv in a lifetime.

16.12.3.2 Other Models

Figure 16.51 plots the excess effect vs. dose, showing four possibilities for how some effect might depend on dose. By definition, there is no excess effect when the dose is zero. The two data points represent the lowest doses at which the effect has been measured. The LNT line is a linear interpolation to zero from these points. Lines are also shown for three other possibilities: (1) a *threshold* below which there is no excess effect, (2) a *supralinear* response, which is higher than predicted by the LNT model, and (3) *hormesis*. In hormesis there is a limited range in which the excess effect is negative—a reduction in the effect. Hormesis has been seen in the response of some organisms to chemicals and in some cases to radiation. Two issues of *Critical Reviews in Toxicology*, Vol. 31 No. 4–5 and Vol. 33, No. 3–4, have been devoted to reviews of hormetic effects in all fields.

Some investigators feel that there is evidence for a threshold dose, and that the LNT model overestimates the risk (Kathren 1996; Kondo 1993; Cohen 2002). Mossman (2001) argues against hormesis but agrees that the LNT model has led to “enormous problems in radiation protection practice” and unwarranted fears about radiation.

On the other hand, annual screening CTs (Brenner and Elliston 2004) and CTs to children (Hall 2002) lead to doses that are large enough so that there is a measured excess risk of developing cancer in an individual; no LNT extrapolation to lower doses is needed. This is shown in Fig. 16.52. A pediatric CT study can lead to a dose in the range of 5–100 mSv. This can be compared with data from the extensive study of 35,000 atomic bomb survivors who have been followed for 70 years. There is a small but statistically significant excess risk of developing cancer.

A concerted effort is underway to reduce the dose from a CT procedure to less than 1 mSv (McCollough et al. 2012).

16.12.4 Radon

The question of a hormetic effect or a threshold effect has received a great deal of attention for the case of radon, where remediation at fairly low radon levels is now recommended. Radon is produced naturally in many types of rock. It is a noble gas, but its radioactive decay products can become lodged in the lung. An excess of lung cancer has been well documented in uranium miners, who have been exposed to fairly high radon concentrations as well as high dust levels and tobacco smoke. Radon at lower concentrations seeps from the soil into buildings and contributes a large fraction of the exposure to the general population. Radon concentrations in the air are measured in the number of radioactive decays per second per cubic meter of air. One *becquerel* (Bq) is one decay per second.

Figure 16.53 shows a study by B. L. Cohen (1995) that plots annual age-adjusted lung-cancer mortality rates in 1601 counties in the USA vs. the average radon concentration measured in that county. The radon concentration is expressed as r/r_0, where r_0 is 37 Bq m^{-3} (1.0 pCi l^{-1} in old units, which will be discussed in the next chapter). The upper two panels are for males, and the lower two are for females. The two panels on the right are corrected for the effects of smoking, using the radon-and-smoking model from BEIR Report V (1990). The dashed lines labeled *Theory* are based on the LNT model. The mortality rate falls with increasing radon concentration, though other studies have shown that it rises at radon concentrations higher than shown here.

Epidemiological studies are difficult and can only be suggestive. A number of authors have criticized Cohen's study for dealing with county-wide averages, and Cohen has defended his results.[27] Cohen argues that his data are valid below about 150 Bq m^{-3}. Lubin (1999) compares an LNT fit and Cohen's model to several other radon studies, shown in Fig. 16.54. The error bars are much larger than in Cohen's figure because the populations are smaller. Lubin argues that this is irrelevant because Cohen has systematic errors. Cohen's data points are not inconsistent with those shown by Lubin. Recall from Table 16.6 that the average annual dose from radon is 2.28 mSv. ICRP (2007) uses the conversion that 600 Bq m^{-3} of radon in a dwelling corresponds to an annual dose of 10 mSv per year. This means that r_0 corresponds to 0.6 mSv per year.

Even if the LNT model for radon is correct, some of our remediation efforts are misdirected. Ayotte et al. (1998) used the LNT model to assess the lung cancer risk from radon in Québec. They predicted a total of 109 deaths from lung

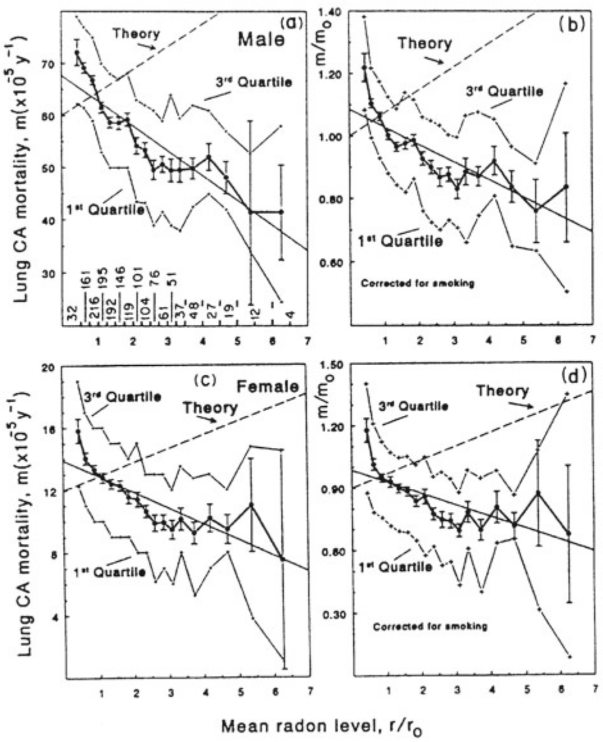

Fig. 16.53 Lung-cancer mortality rates vs. mean radon level in 1601 US counties. Graphs **a** and **b** are for males; (textbfc and **d** are for females. Graphs **b** and **d** have been corrected for smoking levels. Error bars show the standard deviation of the mean. The meaning of radon level is discussed in the text. (From Cohen 1995, pp. 157–174. Used by permission of the Health Physics Society)

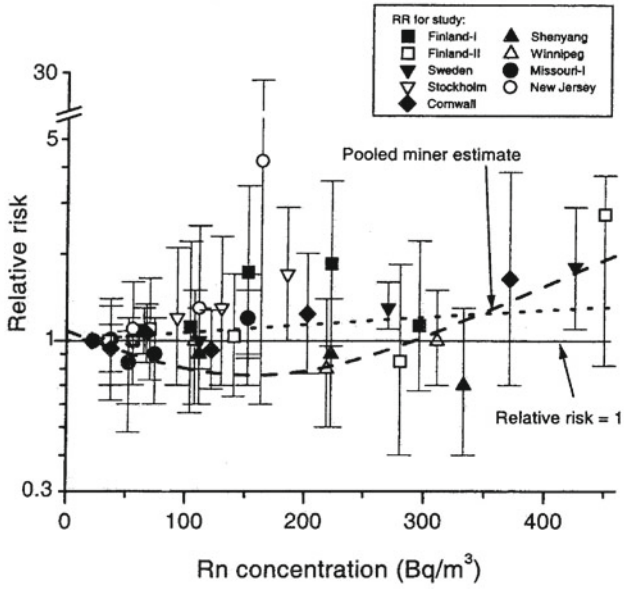

Fig. 16.54 Relative risk (on a log scale) vs. radon concentration. The data points are for several studies, not including Cohen's. The horizontal line shows a relative risk of 1. The dotted line is a linear extrapolation from the miner study. The dashed quadratic line is Cohen's model. (From Lubin 1999, pp. 330–332. Used by permission)

---

[27] For example, see Lubin (1998a); Cohen (1998); Lubin (1998b); Cohen (1999); Lubin (1999), BEIR VI (1999) and Cohen (2007).

cancer in a population of 60,000. Mitigating radon in all residences with concentrations of 200 Bq m^{-3} or more would reduce this number from 109 to 105. The same number of lives would be saved by reducing smoking by 0.04 %.

Symbols Used in Chapter 16

Symbol	Use	Units	First used page
b	Thickness of slice being scanned	m	479
c	Velocity of light	m s^{-1}	467
e	Electron charge	C	464
f	Fraction of photons that interact or detective quantum efficiency		475
f	General function to be represented		478
g	Incremental signal transfer function	kg C^{-1}	466
h	Planck's constant	J s	462
j	Total angular momentum quantum number		461
k	Minimum signal-to-noise ratio		476
k_B	Boltzmann factor	J K^{-1}	469
l	Orbital angular momentum quantum number		461
m	Mass	kg	464
m_e	Mass of electron	kg	467
m	Mean number		475
n	Principal quantum number		461
n	Number of slices in a scan		479
n	Number of moles of a substance	mol	463
n	Number of fractions		484
p	Probability		485
q	Charge	C	464
r	Distance	m	471
r	Risk or probability	varies	493
r, r_0	Radon concentrations	Bq m^{-3}	495
v	Voltage difference	V	468
w	Width of picture element	m	479
w_i	Mass fraction of ith constituent		471
x	Photon energy/electron rest mass energy		467
x, y, z	Coordinates	m	465
A	Proportionality constant	C m^2 kg^{-1}	475
C	Constant	J^{-1} m^{-2}	463
C	Capacitance	F	468
C_{in}	Exposure contrast		474
C_{out}	Brightness contrast		474
D	Absorbed dose	Gy (J kg^{-1})	464
D_0	Reciprocal of proportionality constant α	Gy	482
$D_{R,T}$	Absorbed dose of radiation type R to target organ T	Gy	491
E	Energy	J or eV	462
E	Effective dose to an organ	Sv (J kg^{-1})	491
F	Projection (integral) of f along some direction		478
G	Radiation chemical yield	mol J^{-1}	463
G	Large signal transfer factor	kg C^{-1}	466
H	Hounsfield CT unit		478
H	Dose equivalent	Sv (J kg^{-1})	491
H_E	Effective dose equivalent	Sv	491
H_T	Equivalent dose	Sv (J kg^{-1})	491
K_c	Collision kerma	J kg^{-1}	464
L	Length of object	m	476
N	Number		464
OD	Optical density		465
P	Probability		484
Q	Quality factor		491
R	Resistance	Ohm (Ω)	468
S	Area	m^2	476
S	Surviving fraction		484
S_e(or S_c)	Collision stopping power	J m^{-1}	490
T	Kinetic energy	J	462
T_0	Initial kinetic energy	J	464
T	Optical transmission		465
T	Temperature	K	469
W	Mean energy expended per ion pair formed	J or eV	464
W_R	Radiation weight factor		491
W_T	Tissue weighting factor		491
X	Exposure	C kg^{-1}	464
Z	Atomic number		461
α	Integral of attenuation		478
α	Dose proportionality constant	Gy^{-1}	482
α	Excess risk proportionality constant	Gy^{-1}	493
β	Squared dose proportionality constant	Gy^{-2}	482
γ	Film contrast		465
μ, μ_{atten}	Attenuation coefficient	m^{-1}	471
μ_{en}	Energy absorption coefficient	m^{-1}	464
ν, ν_0	Frequency	Hz	462
ρ	Density	kg m^{-3}	464
σ	Standard deviation		493
Φ	Particle fluence	m^{-2}	463
Φ_T	Particle fluence per unit energy interval	m^{-2} J^{-1} or m^{-2} eV^{-1}	490
Ψ	Energy fluence	J m^{-2}	463

Problems

Section 16.1

Problem 1. Use Eqs. 15.2 and 16.2 to answer the following questions. Then compare your answers to values given in tables, such as those in the *Handbook of Chemistry and Physics*. What is the minimum energy of electrons striking a copper target that will cause the K x-ray lines to appear? What is the approximate energy of the K_α line? Repeat for iodine, molybdenum, and tungsten.

Problem 2. When tungsten is used for the anode of an x-ray tube, the characteristic tungsten K_α line has a wavelength of 2.1×10^{-11} m. Yet a voltage of 69, 525 V must be applied to the tube before the line appears. Explain the discrepancy in terms of an energy-level diagram for tungsten.

Problem 3. Henry Moseley first assigned atomic numbers to elements by discovering that the square root of the frequency of the K_α photon is linearly related to Z. Solve Eq. 16.2 for Z and show that this is true. Plot Z vs. the square root of the frequency and compare it to data you look up.

Problem 4. Equation 16.3b, indicating the number of photons of energy $h\nu$ produced by bremsstrahlung, is known as *Kramer's law*, and is plotted as crosses in Fig. 16.5 (except for the drop at low energies caused by attenuation that is not included in Kramer's law).

(a) Sketch a plot of $d\Phi/dE$ versus energy ($0 < h\nu < h\nu_0$) using Eq. 16.3b.

(b) Use Eq. 16.3b, integrate $d\Phi/dE$ over energy from 0 to $h\nu_0$, and show that Kramer's law predicts that the number of photons goes to infinity if attenuation is not taken into account.

(c) Integrate Eq. 16.3a from 0 to $h\nu_0$ and show that the energy of the bremsstrahlung radiation predicted by Kramer's law is finite, even if the number of photons is infinite. Explain how this is possible. Derive an expression for the total bremsstrahlung energy.

Problem 5.

(a) The energy fluence spectrum for a thin target $d\Psi/d(h\nu)$ in Fig. 16.3 is constant (call it C') for $h\nu < h\nu_0$ and zero for higher energies. Calculate the photon particle fluence rate $d\Phi/d(h\nu)$ and plot it vs. $h\nu$.

(b) Use the chain rule to express the photon particle fluence rate $d\Phi/d\lambda$ for a thin target as a function of wavelength λ and plot it.

(c) Express Eq. 16.3a, giving the energy fluence rate $d\Psi/d(h\nu)$ for a thick target as a function of photon frequency $h\nu$, as an equation for $d\Psi/d\lambda$ as a function of wavelength λ, and plot it.

(d) Repeat the analysis in part (c) for Eq. 16.3b, giving the photon fluence rate $d\Phi/d\lambda$ for a thick target. Plot it.

Section 16.2

Problem 6. A beam of 0.08-MeV photons passes through a body of thickness L. Assume that the body is all muscle with $\rho = 1.0 \times 10^3$ kg m^{-3}. The energy fluence of the beam is Ψ J m^{-2}.

(a) What is the skin dose where the beam enters the body?

(b) Assume the beam is attenuated by an amount $e^{-\mu L}$ as it passes through the body. Calculate the average dose as a function of the fluence, the body thickness, and μ.

(c) What is the limiting value of the average dose as $\mu L \to 0$?

(d) What is the limiting value of the average dose as $\mu L \to \infty$? Does the result make sense? Is it useful?

Problem 7. The obsolete unit, the roentgen (R), is defined as 2.08×10^9 ion pairs produced in 0.001293 g of dry air. (This is 1 cm^3 of dry air at standard temperature and pressure.) Show that if the average energy required to produce an ion pair in air is 33.7 eV (an old value), then 1 R corresponds to an absorbed dose of 8.69×10^{-3} Gy and that 1 R is equivalent to 2.58×10^{-4} C kg^{-1}.

Problem 8. During the 1930s and 1940s it was popular to have an x-ray fluoroscope unit in shoe stores to show children and their parents that shoes were properly fit. These marvellous units were operated by people who had no concept of radiation safety and aimed a beam of x-rays upward through the feet and right at the reproductive organs of the children! A typical unit had an x-ray tube operating at 50 kVp with a current of 5 mA.

(a) What is the radiation yield for 50-keV electrons on tungsten? How much photon energy is produced with a 5-mA beam in a 30-s exposure?

(b) Assume that the x-rays are radiated uniformly in all directions (this is not a good assumption) and that the x-rays are all at an energy of 30 keV. (This is a very poor assumption.) Use the appropriate values for striated muscle to estimate the dose to the gonads if they are at a distance of 50 cm from the x-ray tube. Your answer will be an overestimate. Actual doses to the feet were typically 0.014–0.16 Gy. Doses to the gonads would be less because of $1/r^2$. Two of the early articles pointing out the danger are Hempelmann (1949) and Williams (1949).

Section 16.3

Problem 9. Rewrite Eq. 16.9 in terms of exponential decay of the viewing light and relate the optical density to the attenuation coefficient and thickness of the emulsion.

Problem 10. Derive the useful rule of thumb $\Delta(\text{OD}) = 0.43\gamma\, \Delta X/X$.

Problem 11. The atomic cross-sections for the materials in a gadolinium oxysulfide screen for 50-keV photons are

Element	Cross-section per atom (m^2)	A
Gd	1.00×10^{-25}	157
S	3.11×10^{-27}	32
O	5.66×10^{-28}	16

(a) What is the cross-section per target molecule of GdO_2S?

(b) How many target molecules per unit area are there in a thickness ρdx of material?

(c) What is the probability that a photon interacts in traversing 1.2 kg m^{-2} of GdO_2S?

Problem 12. The film speed is often defined as the reciprocal of the exposure (in roentgens) required to give an optical density that is 1 greater than the base density. Assume that in Fig. 16.6 a relative exposure of 1 corresponds to 10^{-5} C kg^{-1}. Calculate the film speed.

Problem 13. A dose of 1.74×10^{-4} Gy was estimated for part of the body just in front of an unscreened x-ray film. Suppose that a screen permits the dose to be reduced by a factor of 20. Calculate the skin dose on the other side of the body (the entrance skin dose) assuming 50-keV photons and a body thickness of 0.2 m. Ignore buildup, and assume that only unattenuated photons are detected.

Problem 14. Find an expression for photon fluence per unit absorbed dose in a beam of monoenergetic photons. Then find the photon fluence for 50-keV photons that causes a dose of 10^{-5} Gy in muscle.

Problem 15. A dose of 100 Gy might cause noticeable radiation damage in a sodium iodide crystal. How long would a beam of 100-keV photons have to continuously and uniformly strike a crystal of 1-cm^2 area at the rate of 10^4 photon s^{-1}, in order to produce this absorbed dose? For NaI, $\mu_{\text{en}}/\rho = 0.1158\ \text{m}^2\ \text{kg}^{-1}$.

Problem 16. Another method to measure the absorbed dose is by calorimetry. Show that if all the energy imparted warms the sample, the temperature rise is 2.39×10^{-4} °C per Gy.

Section 16.4

Problem 17. Plot μ for lead, iodine, and barium from 10 to 200 keV.

Problem 18. Use a spreadsheet to make the following calculations. Consider a photon beam with 100 kVp.

(a) Use Eq. 16.3b to calculate the photon fluence from a thick target at 1, 10, 20, 30, 40, 50, 60, 70, 80, 90, and 100 keV.

(b) The specific gravity of aluminum is 2.7. Make a table of the photon fluence at these energies emerging from 2 and 3 mm of aluminum. Compare the features of this table to Fig. 16.15.

(c) Use trapezoidal integration to show that the average photon energy is 44 keV after 2-mm filtration and 47 keV after 3-mm filtration.

(d) Repeat for 120 kVp and show that the average energies after the same filtrations are 52 and 55 keV.

Problem 19. To get a qualitative understanding of Fig. 16.15, assume the photon particle fluence is given by Eq. 16.3b multiplied by a factor $exp(-BL/(h\nu)^3)$, where B is a constant, L is the thickness of the aluminum filtration (in cm) and the $1/(h\nu)^3$ dependence on the photon energy (in keV) arises from the photoelectric cross-section energy dependence, Eq. 15.8.

(a) What are the units of B?

(b) Use some simple numerical method to estimate B from Fig. 16.15. One method might be to calculate the maximum of the photon fluence curve and adjust B so the maximum occurs at the correct photon energy.

(c) For the value of B you found in part (b), plot the three relative photon fluence curves as a function of photon energy, as shown in Fig. 16.15. Normalize the curves so the peak of the 0.1-cm filtration curve is equal to 1.

Problem 20. X-ray beams have a spectrum of photon energies. It would be very laborious to measure the spectrum every time we want to check the quality of the beam. In addition to kVp, one simple measurement that is used to check beam quality (related to the energy spectrum) is the *half-value layer* HVL–the thickness of a specified absorber (often Cu or Al) that reduces the intensity of the beam to one-half.

(a) For a monoenergetic beam, relate HVL to the attenuation coefficient. What is the HVL if the attenuation coefficient is $0.46\,\text{mm}^{-1}$?

(b) For a monoenergetic beam, how does the quarter-value layer QVL relate to HVL?

(c) Suppose a beam has equal numbers of photons at two different energies. The attenuation coefficients at these energies are $0.46\,\text{mm}^{-1}$ and $0.6\,\text{mm}^{-1}$. Find the HVL and QVL for this beam. You may need to plot a graph or use a computer algebra program.

Problem 21. The half value layer (HVL) is often used to characterize an x-ray beam. It is the thickness of a specified absorber that attenuates the beam to one-half the original value. Figure 16.41 refers to a beam with a 3.0 mm Cu HVL. What is the value of the attenuation coefficient? What monoenergetic x-ray beam does this correspond to?

Problem 22. Assume an antiscatter grid is made of lead sheets 3-mm long with a spacing between sheets of 0.3 mm. Ignore the thickness of the sheets. If all photons hitting the sheets are absorbed, what is the largest angle from the incident beam direction that a photon can be scattered and still emerge?

Section 16.5

Problem 23. Suppose that two measurements are made: one of the combination of signal and noise, $y = s + n$, and one of just the noise n. One wishes to determine $s = y - n$.

(a) Find $s - \bar{s}$ in terms of y, $\bar{y}$, n, and $\bar{n}$.

(b) Show that if y and n are uncorrelated, $\overline{(s-\bar{s})^2} = \overline{(y-\bar{y})^2} + \overline{(n-\bar{n})^2}$ and state the mathematical condition for being uncorrelated.

(c) If y and n are Poisson distributed, under what conditions is the $\sqrt{2}$ factor of Footnote 13 needed?

Section 16.7

Problem 24. A molybdenum target is used in special x-ray tubes for mammography. The electron energy levels in Mo are as follows:

K	20 000 eV	L_{I}	2886 eV	M_{I}	505 eV
		L_{II}	2625 eV	M_{II}	410 eV
		L_{III}	2520 eV	M_{III}	392 eV
				M_{IV}	230 eV
				M_{V}	227 eV

What is the energy of the K_α line(s)? The K_β line(s) (defined in Fig. 16.2)?

Problem 25. As a simple model for mammography, consider two different tissues: a mixture of 2/3 fat and 1/3 water, with a composition by weight of 12 % hydrogen, 52 % carbon and 36 % oxygen; and glandular tissue, composed of 11 % hydrogen, 33 % carbon, and 56 % oxygen. The density of the fat and water combination is 940 kg m^{-3}, and the density of glandular tissue is 1020 kg m^{-3}. What is the attenuation in 1 mm of the fat-water combination and in 1 mm of glandular tissue for 50-keV photons? For 30-keV photons?

Section 16.8

Problem 26. It is often said that the number of photons that must be detected in order to measure a difference in fluence with a certain resolution can be calculated from $N = (\Delta\Phi/\Phi)^{-2}$. (For example, if we want to detect a change in Φ of 1 % we would need to count 10^4 photons.) Use Eq. 16.20 to make this statement more quantitative. Discuss the accuracy of the statement.

Problem 27. Spiral CT uses interpolation to calculate the projections at a fixed value of z before reconstruction. This has an effect on the noise. Let σ_0 be the noise standard deviation in the raw projection data and σ be the noise in the interpolated data. The interpolated signal, α, is the weighted sum of two values: $\alpha = w\alpha_1 + (1-w)\alpha_2$.

(a) Show that the variance in α is $\sigma^2 = w^2\sigma_0^2 + (1-w)^2\sigma_0^2$. Plot σ/σ_0 vs. w.

(b) Averaging over a 360° scan involves integrating uniformly over all weights:

$$\sigma^2 = \int_0^1 \left[w^2\sigma_0^2 + (1-w)^2\sigma_0^2 \right] dw.$$

Find the ratio σ/σ_0.

Problem 28. An experimental technique to measure cerebral blood perfusion is to have the patient inhale xenon, a noble gas with $Z = 54$, $A = 131$ (Suess et al. 1995). The solubility of xenon is different in red cells than in plasma. The equation used is

$$(\text{arterial enhancement}) = \frac{5.15\theta_{\mathrm{Xe}}}{(\mu/\rho)_w/(\mu/\rho)_{\mathrm{Xe}}} C_{\mathrm{Xe}}(t),$$

where the arterial enhancement is in Hounsfield units, C_{Xe} is the concentration of xenon in the lungs (end tidal volume), and

$$\theta_{\mathrm{Xe}} = (0.011)(\mathrm{Hct}) + 0.10.$$

Hct is the *hematocrit*: the fraction of the blood volume occupied by red cells. Discuss why the equation has this form.

Section 16.9

Problem 29. Use Equations 16.30 and 16.31 to derive an expression for the probability of eradicating a tumor (no surviving tumor cells) as a function of dose for tumors containing different numbers of cells. Verify that your expression reproduces Fig. 16.38.

Section 16.10

Problem 30. Geiger's rule is an approximation to the range-energy relationship:

$$R = AE^p.$$

For protons in water $A = 0.0022$ when R is in cm and E is in MeV. The exponent $p = 1.77$. This is a good approximation for $E < 200$ MeV. Use Geiger's approximation to find dE/dx as a function of R for 100 MeV protons. Make a plot to show the Bragg peak when straggling is ignored.

Problem 31. Assume the stopping power of a particle, $S = -dT/dx$, as a function of kinetic energy, T, is $S = C/T$.

(a) What are the units of C? From Fig. 15.17, estimate for protons the range of kinetic energies over which $S = C/T$ is appropriate.

(b) If the initial kinetic energy at $x = 0$ is T_0, find $T(x)$.

(c) Determine the range R of the particle as a function of C and T_0. For protons in water, estimate C from Fig. 15.26.

(d) Plot $S(x)$ vs. x. Compare the shape of the curve to Fig. 16.47. Does this plot contain a Bragg peak?

(e) Discuss the implications of the shape of $S(x)$ for radiation treatment using this particle.

Section 16.11

Problem 32. Calculate $(\overline{S}_e/\rho)_g^w$ in argon for 0.1-, 1.0- and 10-MeV electrons. The values of S_e/ρ for argon at these energies are 2.918, 1.376, and 1.678 $\mathrm{cm}^2\ \mathrm{g}^{-1}$.

Problem 33. An ion chamber contains 10 cm^3 of air at standard temperature and pressure. Find q vs. D for 0.5-MeV electrons.

Section 16.12

Problem 34. Suppose that the probability p per year of some event (death, mutations, cancer, etc.) consists of a spontaneous component S and a component proportional to the dose of something else, D: $p = S + AD$. The dose may be radiation, chemicals, sunlight, etc. Investigations of women given mammograms showed that if p is the probability of acquiring breast cancer, $S = 1.91 \times 10^{-3}$ and $A = 4 \times 10^{-4}$ Gy^{-1}. How many women had to be studied to distinguish between $A = 0$ and the value above if $D = 2$ Gy? If $D = 10^{-2}$ Gy?

References

AAPM Report 87 (2005) Diode in vivo dosimetry for patients receiving external beam radiation therapy. American Association of Physicists in Medicine, College Park. Report of Task Group 62 of the Radiation Therapy Committee

AAPM Report 96 (2007) The measurement, reporting and management of radiation dose in CT. American Association of Physicists in Medicine, College Park. Report of Task Group 23 of the Diagnostic Imaging Council CT Committee

Alberts B et al (2002) Molecular biology of the cell, 4th edn. Garland, New York, p 230

Armato SG, van Ginneken B (2008) Anniversary paper: image processing and manipulation through the pages of Medical Physics. Med Phys 35:4488–4500

Attix FH (1986) Introduction to radiological physics and radiation dosimetry. Wiley, New York

Ayotte P, Lévesque B, Gauvin D, McGregor RG, Martel R, Gingras S, Walker WB, Létourneau E G (1998) Indoor exposure to ^{222}Rn: a public health perspective. *Health Phys* 75(3):297–302

Barth RF (2003) A critical assessment of boron neutron capture therapy: an overview. J Neurooncol 62:1–5. (The entire issue of the journal is devoted to a review of BNCT)

BEIR Report V (1990) Health effects of exposure to low levels of ionizing radiation. National Academy Press, Washington, DC. (Committee on the Biological Effects of Ionizing Radiation)

BEIR Report VI (1999) Health effects of exposure to radon. National Academy Press, Washington, DC. (Committee on Health Risks of Exposure to Radon)

BEIR Report VII (2005) Health risks from exposure to low levels of ionizing radiation. National Academy Press, Washington, DC. (Committee to Assess Health Risks from Exposure to Low Levels of Ionizing Radiation)

Birch R, Marshall M (1979) Computation of bremsstrahlung X-ray spectra and comparison with spectra measured with a Ge(Li) detector. Phys Med Biol 24:505–517

Boice JD Jr (1996) Risk estimates for radiation exposures. In: Hendee WR, Edwards FM (eds). Health effects of exposure to low-level ionizing radiation. Institute of Physics, Bristol.

Brenner DJ, Elliston CD (2004) Estimated radiation risks potentially associated with full-body CT screening. Radiology 232:735–738

Broad WJ (1980) Riddle of the Nobel debate. Science 207:37–38

Brooks AL (2003) Developing a scientific basis for radiation risk estimates: goal of the DOE low dose research program. Health Phys 85(1):85–93

Brooks RA, DiChiro G (1976a) Principles of computer assisted tomography (CAT) in radiographic and radioisotope imaging. Phys Med Biol 21:689–732

Brooks RA, DiChiro G (1976b) Statistical limitations in x-ray reconstructive tomography. Med Phys 3:237–240

Cohen BL (1995) Test of the linear—no threshold theory of radiation carcinogenesis for inhaled radon decay products. Health Phys 68(2):157–174

Cohen BL (1998) Response to Lubin's proposed explanations of our discrepancy. Health Phys 75(1):18–22

Cohen BL (1999) Response to the Lubin rejoinder. Health Phys 76(4):437–439

Cohen, B. L. (2002). Cancer risk from low-level radiation. [see comment]. AJR Am J Roentgenology 179(5):1137–1143

Cohen BL (2007) The cancer risk from low-level radiation (Chapter 3). In: Tack D, Gevenois PA (eds) Radiation dose from adult and pediatric multidetector computed tomography. Springer, Berlin

Cormack AM (1980) Nobel award address: early two-dimensional reconstruction and recent topics stemming from it. Med Phys 7(4):277–282

Cowen AR, Davies AG, Sivananthan MU (2008a) The design and imaging characteristics of dynamic, solid-state, flat-panel x-ray image detectors for digital fluoroscopy and fluorography. Clin Radiol 63:1073–1085

Cowen AR, Kengyelics SM, Davies AG (2008b) Solid-state, flat-panel, digital radiography detectors and their physical imaging characteristics. Clin Radiol 63:487–498

Delaney TF, Kooy HM (2008) Proton and charged particle radiotherapy. Williams and Wilkins, Philadelphia

DeVita VT (2003) Hodgkin's disease—Clinical trials and travails. N Engl J Med 348(24):2375–2376

DiChiro G, Brooks RA (1979) The 1979 Nobel prize in physiology or medicine. Science 206:1060–1062

Doi K (2006) Diagnostic imaging over the last 50 years: research and development in medical imaging science and technology. Phys Med Biol 51:R5–R27

Doss M, Little MP, Orton C (2014) Point/Counterpoint: low-dose radiation is beneficial, not harmful. Med Phys 41:070601. doi:http://dx.doi.org/10.1118/1.4881045

Douglas JG, Koh WJ, Austin-Seymour M, Laramore GE (2003) Treatment of salivary gland neoplasms with fast neutron radiotherapy. Arch Otolaryngol Head Neck Surg 129(9):944–948

Duncan W (1994) An evaluation of the results of neutron therapy trials. Acta Oncol 33(3):299–306. (This issue of the journal is devoted to fast-neutron therapy)

Goitein M (2008) Radiation oncology: a physicist's eye view. Springer, New York

Hall EJ (2000) Radiobiology for the radiologist, 5th edn. Lippincott Williams & Wilkins, Philadelphia

Hall EJ (2002) Helical CT and cancer risk: introduction to session I. Pediatr Radiol 32:225–227

Hall EJ (2003) The bystander effect. Health Phys 85(1):31–35

Hall EJ, Giaccia AJ (2012) Radiobiology for the radiologist, 7th edn. Lippincott Williams & Wilkins, Philadelphia

Harris CC, Hamblen DP, Francis JE Jr (1969) Basic Principles of Scintillation Counting for Medical Investigators. ORNL-2808

Health Physics Society (2010) Radiation risk in perspective. Position statement of the health physics society. http://hps.org/hpspublications/positionstatements.html./risk ps010-2.pdf

Hempelmann LH (1949) Potential dangers in the uncontrolled use of shoe fitting fluoroscopes. N Engl J Med 241:335–336

Hendee WR, Ritenour ER (2002) Medical imaging physics, 4th edn. Wiley-Liss, New York

Higson DJ (2004) The bell tolls for LNT. Health Phys 87(Supplement 2):S47–S50

Hogstrom KR, Almond PR (2006) Review of electron beam therapy physics. Phys Med Biol 51:R455–489

Hounsfield GN (1980) Nobel award address: computed medical imaging. Med Phys 7(4):283–290

Hubbell JH, Seltzer SM (1996) Tables of x-ray mass attenuation coefficients and mass energy-absorption coefficients from 1 keV to 20 MeV for elements Z=1 to 92 and 48 additional substances of dosimetric interest. National Institute of Standards and Technology Report NISTIR 5632. http://www.nist.gov/pml/data/xraycoef

Hunt DC, Kirby SS, Rowlands JA (2002) X-ray imaging with amorphous selenium: x-ray to charge conversion gain and avalanche multiplication gain. Med Phys 29(11):2464–2471

ICRP (1991) The 1990 recommendations of the international commission on radiological protection. Ann ICRP 21:1–3

ICRP (2007) The 2007 recommendations of the international commission on radiation protection. Ann ICRP Publication No. 103. Elsevier, New York

ICRU Report 31 (1979) Average energy required to produce an ion pair. International Commission on Radiation Units and Measurements, Bethesda

ICRU Report 33 (1980, Reprinted 1992). *Radiation Quantities and Units*. Bethesda, MD, International Commission on Radiation Units and Measurements.

ICRU Report 37 (1984) Stopping powers for electrons and positrons. International Commission on Radiation Units and Measurements, Bethesda

ICRU Report 39 (1985) Determination of dose equivalents resulting from external radiation sources. International Commission on Radiation Units and Measurements, Bethesda

ICRU Report 41 (1986) Modulation transfer function of screen-film systems. International Commission on Radiation Units and Measurements, Bethesda

ICRU Report 54 (1996) Medical imaging—the assessment of image quality. International Commission on Radiation Units and Measurements, Bethesda

ICRU Report 74 (2005) Patient dosimetry for x rays used in medical imaging. J ICRU 5(2):1–113

Kalender WA (2011) Computed tomography: fundamentals, system technology, image quality and applications, 3rd edn. Publicis, Erlangen

Kassis AI (2004) The amazing world of Auger electrons. Rad Biol 80(11–12):789–803

Kathren RL (1996) Pathway to a paradigm: the linear nonthreshold dose-response model in historical context: the American Academy of Health Physics 1995 Radiology Centennial Hartman Oration. Health Phys 70(5):621–635

Khan FM (1986) Clinical electron beam dosimetry. In Keriakes JG, Elson HR, Born CG (eds) Radiation oncology physics. American Association of Physicists in Medicine, College Park

Khan FM (2003) The physics of radiation therapy, 3rd edn. Philadelphia, Lippincott Williams & Wilkins, p 163, 204, 210, 215

Khan FM (2010) The physics of radiation therapy, 4th edn. Lippincott Williams & Wilkins, Philadelphia

Kondo S (1993) Health effects of low-level radiation. Kinki University Press, Osaka. English translation: Medical Physics, Madison

Körner M, Weber CH, Wirth S, Pfeifer K-J, Reiser MF, Treitl M (2007) Advances in digital radiography: physical principles and system overview. Radiographics 27:675–686

Lubin JH (1998a) On the discrepancy between epidemiologic studies in individuals of lung cancer and residential radon and Cohen's ecologic regression. Health Phys 75(1):4–10

Lubin JH (1998b) Rejoinder: Cohen's response to "On the discrepancy between epidemiologic studies in individuals of lung cancer and residential radon and Cohen's ecologic regression". Health Phys 75(1):29–30

Lubin JH (1999) Response to Cohen's comments on the Lubin rejoinder. Health Phys 77(3):330–332

Lutz G (1999) Semiconductor radiation detectors. Springer, New York

Macovski A (1983) Medical imaging systems. Prentice-Hall, Englewood Cliffs

McCollough CH, Schueler BA (2000) Educational treatise: calculation of effective dose. Med Phys 27(5):828–837

McCollough CH, Chen GH, Kalender W, Leng S, Samei E, Taguchi K, Wang G, Yu L, Pettigrew RI (2012) Achieving routine submillisievert CT scanning: report from the summit on management of radiation dose in CT. Radiology 264(2):567–580

Mettler FA, Huda W, Yoshizumi TT, Mahesh M (2008) Effective doses in radiology and diagnostic nuclear medicine: a catalog. Radiology 248:254–263

Metz CE, Doi K (1979) Transfer function analysis of radiographic imaging systems. Phys Med Biol 24(6):1079–1106

Miralbell R, Lomax A, Cella L, Schneider U (2002) Potential reduction of the incidence of radiation-induced second cancers by using proton beams in the treatment of pediatric tumors. Int J Radiat Oncol Biol Phys 54(3):824–829

Mossman KL (2001) Deconstructing radiation hormesis. Health Phys 80(3):263–269

NCRP Report 94 (1987) Exposure of the population in the United States and Canada from natural background radiation. National Council of Radiation Protection and Measurements, Bethesda

NCRP Report 100 (1989) Exposure of the U.S. population from diagnostic medical radiation. National Council of Radiation Protection and Measurements, Bethesda

NCRP Report 136 (2001) Evaluation of the linear-nonthreshold dose-response model for ionizing radiation. National Council of Radiation Protection and Measurements, Bethesda

NCRP Report 160 (2009) Ionizing radiation exposure of the population of the United States. National Council on Radiation Protection and Measurements, Bethesda

Orton C (1997) Fractionation: radiobiological principles and clinical practice (Chapter 21). In: Khan FM, Gerbi B (eds) Treatment planning in radiation oncology. Williams and Wilkins, Baltimore

Pisano ED, Yaffe MJ (2005) Digital mammography. Radiology 234:353–362

Platzman RL (1961) Total ionization in gases by high-energy particles: an appraisal of our understanding. Intl J Appl Radiat Is 10:116–127

Ratliff ST (2009) Resource letter MPRT-1: medical physics in radiation therapy. Am J Phys 77:774–782

Rowlands JA (2002) The physics of computed radiography. Phys Med Biol 47: R123–R126

Schlomka JP, Roessl E, Dorscheid R, Dill S, Martens G, Istel T, Bäumer C, Herrmann C, Steadman R, Zeitler G, Livne A, Proksa R (2008) Experimental feasibility of multi-energy photon-counting K-edge imaging in pre-clinical computed tomography. Phys Med Biol 53:4031–4047

Schulz RJ, Kagan AR (2002) On the role of intensity-modulated radiation therapy in radiation oncology. Med Phys 29(7):1473–1482

Shani G (1991) Radiation dosimetry: instrumentation and methods. CRC, Boca Raton

Shani G (2001) Radiation dosimetry: instrumentation and methods, 2nd edn. CRC, Boca Raton

Smith AR (2009) Vision 20/20: proton therapy. Med Phys 36:556–568

Sobol WT (2002) High frequency x-ray generator basics. Med Phys 29(2):132–144

Steel GG (1996) From targets to genes: a brief history of radiosensitivity. Phys Med Biol 41(2):205–222

Suess C, Polacin A, Kalender WA (1995) Theory of xenon/computed tomography cerebral blood flow methodology. In: Tomonaga M, Tanaka A, Yonas H (eds). Quantitative cerebral blood flow measurements using stable xenon/CT: clinical applications. Futura, Armonk

Suit H, Urie M (1992) Proton beams in radiation therapy. J Natl Cancer Inst 84(3):155–164

Tack D, Gevenois PA (eds) (2007) Radiation dose from adult and pediatric multidetector computed tomography. Springer, Berlin

Tubiana M, Feinendegen LE, Yang C, Kaminski JM (2009) The linear no-threshold relationship is inconsistent with radiation biologic and experimental data. Radiology 251:13–22

Uffmann M, Schaefer-Prokop C (2009) Digital radiography: the balance between image quality and required radiation dose. Eur J Radiol 72:202–208

Upton AC (2003) The state of the art in the 1990's: NCRP report no. 136 on the scientific bases for linearity in the dose-response relationship for ionizing radiation. Health Phys 85(1):15–22

van Eijk CWE (2002) Inorganic scintillators in medical imaging. Phys Med Biol 47:R85–R106

Wagner HN Jr (ed) (1968) Principles of nuclear medicine. Elsevier, p 153, 162

Wagner RF (1977) Toward a unified view of radiological imaging systems. Part II: Noisy images. Med Phys 4(4):279–296

Wagner RF (1983) Low contrast sensitivity of radiologic, CT, nuclear medicine, and ultrasound medical imaging systems. IEEE Trans Med Imaging MI-2(3):105–121

Wagner RF, Weaver KE, Denny EW, Bostrom RG (1974) Toward a unified view of radiological imaging systems. Part I: Noiseless images. Med Phys 1(1):11–24

Williams CR (1949) Radiation exposures from the use of shoe-fitting fluoroscopes. N Engl J Med 241:333–335

William TM, James DC (1989) Radiation Oncology, 6th edn. Mosby, St. Louis

Xu XG, Bednarz B, Paganetti H (2008) A review of dosimetry studies on external-beam radiation treatment with respect to second cancer induction. Phys Med Biol 53:R193–R241

Yu CX, Amies CJ, Svatos M (2008) Planning and delivery of intensity-modulated radiation therapy. Med Phys 35:5233–5241